Surface Science 630 (2014) 46–63

Contents lists available at ScienceDirect

Surface Science

journal homepage: www.elsevier.com/locate/susc

Structure and reactivity of zero-, two- and three-dimensional Pd supported on $SrTiO_3(001)$

S.E. Stoltz [a], D.E. Ellis [b,*], M.J. Bedzyk [a]

[a] Dept. of Materials Science and Engineering, Northwestern University, Evanston, IL 60208, United States
[b] Dept. of Physics and Astronomy, Northwestern University, Evanston, IL 60208, United States

ARTICLE INFO

Article history:
Received 13 April 2014
Accepted 23 June 2014
Available online 1 July 2014

Keywords:
Supported Pd nanoparticles
Particle–substrate interaction
Density functional calculation
Molecule adsorption on particle
Strontium titanate substrate

ABSTRACT

Interactions of Pd atoms, films and nanoparticles with a $SrTiO_3(001)$ substrate are studied via first principles Density Functional Theory. Effects of the substrate upon structural, electronic and chemical properties of the supported Pd are considered. By comparison of different experimentally observed particle shapes and orientation, and with atomic and planar Pd adsorbates, some detailed understanding is obtained about particle–support interactions. Adsorption of atoms (H, C, O) and small molecules (OH, CO, CH_3) is used as a probe of chemical activity of different faces, edges and vertices of the particles.

1. Introduction

Metallic nanoparticles supported on refractory oxides are known to be useful catalysts, especially for oxidation of organic molecules. Particle–support interactions have been shown to contribute to catalyst performance by stabilizing particle size and dispersion, as well as controlling chemical selectivity and reactivity. There appears to be a consensus that the presence of specific particle facets, edges and vertices is beneficial, perhaps essential to both catalytic selectivity and activity. With respect to particle–substrate interaction, one frequently speaks of the importance of 'triple-points' at the intersection of catalytic particle, its support, and the gas phase medium conducting reactive molecules. Seen as a composite, the particle–oxide interface can provide catalytic sites not available in either component separately. As a recent example, the epitaxial match between Pt(110) and the (100) crystal plane of $SrTiO_3$ (STO) has been shown to impart exceptional stability and preferred metal surface orientation to Pt nanoparticles produced by Atomic Layer Deposition (ALD) on both crystal surfaces and nanocubes [1,2]. High resolution electron microscopy has shown detailed shapes and facets of Pd nanoparticles, which depend upon temperature and growth conditions, as well as the stage of reconstruction of the STO surface [3]. Further work on Ag:STO(100) shows the generality of growth and stability over a number of catalytically important metals [4]. The present work is dedicated to theoretical modeling and analysis which could elucidate specific aspects of particle–substrate interactions and their impact on gas-phase adsorption of atoms and small molecules. The ability to understand and control these interactions, along with surface preparation such as partial hydroxylation, could lead to optimized catalytic properties.

Space does not permit an adequate review of the rich theoretical and experimental literature on Pd particles, films, and overlayers. Some relevant examples will be cited to place the present work in perspective. Palladium metal in its *fcc* phase is reasonably well described by Density Functional Theory (DFT), in a periodic band structure model. The lattice parameter a_0 found as ($3.84 < 3.89 < 3.95$ Å) in DFT-LDA, experiment, and DFT-GGA/PBE approaches [5], showing characteristic under- and over-estimates of interatomic distances arising from use of simple Local Density Approximation (LDA) and more elaborate (e.g., GGA/PBE) exchange and correlation functionals. The cohesive energy E_{coh} appears as ($3.68 < 3.94 < 5.08$ eV/atom) in the order GGA/PBE < expt < LDA showing the usual overbinding of LDA compared to GGA/PBE. Further comparisons of properties like bulk modulus, vibrational frequencies, and magnetic moments can be usefully made. For the present purposes it is worth noting that in comparing *trends* of a given property among similar systems the differences between various DFT functionals are often unimportant. The models evaluated in the present work are all based upon the Perdew–Wang GGA/PW91 functional, which has been widely applied in solid state and surface studies. Within this scheme, the STO bulk lattice constant was calculated as 3.94 Å, and for bulk Pd 3.954 Å. The calculated STO substrate

* Corresponding author.
E-mail address: don-ellis@northwestern.edu (D.E. Ellis).

http://dx.doi.org/10.1016/j.susc.2014.06.018
0039-6028/

structure is in very good agreement with experiment, 3.9051 Å, while the larger deviation for Pd (experimental 3.89 Å) is consistent with previous calculations [6].

Unsupported Pd_N particles with $38 \leq N \leq 4874$ atoms were reported by Qi et al. [7] using Molecular Dynamics (MD) with a semiempirical potential parametrized to bulk. Showing the value of judicious use of fitted potential data, they find that E_{coh} trends toward 3.8 eV/atom with increasing size, and that the particle energy scales nicely with $N^{-1/3}$ as expected for a classical surface energy. Nava et al. [8] carried out DFT-BP/86 calculations for $2 \leq N \leq 309$ confirming the quantum-mechanical $N^{-1/3}$ trend line of binding energy, with distinct deviations for highly favored or unfavored bonding structures. They extrapolated a bulk value of E_{coh} of 3.59 eV/atom with the theoretical underestimate being attributed partially to limited basis sets, and to the particular choice of functional. Parenthetically, the authors noted that the B3LYP functional popular with chemists does rather poorly in describing metal particles. Combining semiempirical potentials and a genetic algorithm, followed by DFT structural refinements, Rogan et al. [9] considered clusters with $14 \leq N \leq 21$, showing the benefits of a hybrid classical/quantum methodology. They further demonstrated that several different computational methodologies give closely similar results, providing some confidence in derived properties. In particular they found that small particle nearest-neighbor (NN) distances d_{nn} are characteristically smaller than bulk (2.85 Å), particularly near the particle surface (2.63–2.66 Å for Pd_{21}). In contrast with the superparamagnetic nature of bulk Pd, small particles were found to be magnetic, with moment per atom increasing with particle size.

Let us pass over Pd surface properties, and take up the subject of films, overlayers, and adsorption on Pd. In a Monte Carlo/Molecular Dynamics (MC/MD) approach using the semiempirical Embedded Atom Method (EAM) Bolding and Carter [10] investigated the lattice-strain driven *bcc* → *fcc* transformation of a Pd thin film supported on a *bcc* (110) substrate. While a somewhat overestimated E_{coh} of 4.2 eV/atom was obtained, this work pointed the direction toward more rigorous surface film structure investigations. In another pioneering work Tomanek et al. [11] considered the adsorption of hydrogen on Pd(001) and (110) surfaces, using the DFT-LDA scheme. They predicted a most stable 4-fold site, with an adsorption energy of 2.92 eV/atom in reasonable agreement with experiment (2.77 eV). Further, in this site H was found to sit 0.24 Å above the surface plane, compared to the experimental value of 0.30 Å, and identified as being very similar to the octahedral H-binding site in the bulk compound PdH.

Ochs et al. [12] exploited the very favorable cube-on-cube orientation of *fcc* Pd supported on $SrTiO_3$ (001) (STO). Using a DFT mixed basis pseudopotential band structure method, they considered one- and two-monolayer (ML) coverage by Pd, on ideal TiO_2 and SrO terminations. Among other properties, they found a work of separation W_{sep} of overlayer relative to separated Pd film and STO structures of 1.67 J/m^2 for 1 ML with Pd atop oxygen on the TiO_2 termination, which is energetically favored over the SrO face. The Pd – O bond length in this case was predicted as 2.14 Å. Ochs and Elsässer further considered (002) Pd films on STO(100) with similar results, noting that 3 ML films already resemble a sharp interface between STO and bulk Pd [13].

Finally we turn to the catalytically important case of metal particles supported on an oxide surface. In a remarkable example of single-atom catalysis, Abbet et al. carried out experimental and theoretical analyses of Pd_1 trapped at an MgO surface F-center (oxygen vacancy) [14]. They found the surface complex to be highly selective for the cyclotrimerization of acetylene to benzene, and also forming CO_2 via $Pd(CO)_2(O_2)$ and $Pd(CO_3)(CO)$ precursors. Hoffmann et al. carried out DFT calculations on CO chemisorption on octahedral fragments of bulk Pd with O_h symmetry constraints, concluding that strongest binding occurs at cluster edge bridge positions [15]. Infrared vibrational spectra on alumina-supported Pd particles were used to interpret the results in terms of *bridge*-bonded CO at edges and defects. No attempt was made to identify particle–support interactions. Piccolo and Henry carried out experimental studies of CO–NO reactions on MgO(100), finding that particles with a larger number of (111) facets are more reactive [16]. They further considered that pre-adsorption (physisorption) of NO on the substrate plays an important role in the reaction kinetics. Tait et al. studied methane adsorption and dissociation and oxygen adsorption and reaction with CO on Pd nanoparticles on MgO(100) and on Pd(111) [17] using molecular beam techniques. They found that CH_4 binds more strongly to particles than to the (111) surface, and that O_2 adsorption on particles follows a precursor adsorbed on the MgO substrate. In order to determine the sticking probability for reactive dissociation of CH_4 they adopted a generally accepted equilibrium particle geometry of a truncated half octahedron with a height/base ratio of 0.4. The authors conclude that if this model is correct, the particles are about twice as reactive as the Pd(111) surface.

A large number of experimental and theoretical studies have been made on *metal*:MgO(100) interactions, of which we may cite a few [18]. MgO is a favorable substrate for surface science studies due to its simple rock-salt structure, rather stable (100) surface with a controllable minimum of defects, mostly oxygen vacancies. The clean surface is rather unreactive, and has found limited use as a catalyst support. With a cubic lattice constant of 4.208 Å, atomic coverage up to several monolayers of coinage metals Cu, Au, Ag, and Pd, Pt among others, have been achieved. The poor metal–oxide lattice match results in high metal diffusivity on the surface. In a comparative study of Cu on MgO(001) and on the perovskite $BaTiO_3$(001) (BTO) surfaces it was found that the better lattice match and stronger binding interaction with BTO could lead to interesting catalytic properties [19].

Catalytic supports are often selected for their high surface area, thermal, chemical, and mechanical stability; further, the support can also affect the selectivity and reactivity of the catalyst [20]. Sinfelt and coworkers [21] have shown that different supports can greatly alter the catalytic behavior. An ideal support would stabilize a nanoparticle catalyst with the desired exposed faces, resistent to cluster agglomeration and diffusion at operating temperature. Such a catalyst could take advantage of the differences in selectivity and reactivity of different faces which have been found on oriented single crystals [22]. The many attempts to do this over the last decades using kinetic control of the nanoparticle shape have given only temporary improvement since the active facets on the nanoparticles were thermodynamically unstable in the Wulff construction [23]. Richter and Wagner imaged the growth of 3D Pd particles on STO(001) using Scanning Tunneling Microscopy; no structural details were resolved [24]. Atomic layer deposition (ALD) methodology offers a relatively recent approach to highly controlled metal deposition, resulting for example, in Pt films and particles on single crystal STO(001) and STO nanocubes. AFM, SEM, and GISAXS measurements permitted the study of early stages of the nucleation and growth of uniformly sized Pt nanoparticles [1]. ALD Pt nanoparticles on high surface area nanocubes with predominantly (001) exposed facets were prepared [2], and characterized using electron microscopy, small-angle and wide-angle X-ray scattering, X-ray absorption spectroscopy and theory [25]. The Pt_N/STO nanocube catalysts have a >50 °C lower light-off temperature for propane oxidation than a conventional Pt/Al_2O_3 catalyst, turn over frequencies up to 3 orders of magnitude higher, and show improved resistance to deactivation [26]. This material demonstrates [27] that by exploiting the epitaxy of Pt on STO(001) one can obtain stable nanoparticles with different surface facets from those obtained using a polycrystalline substrate. While the equilibrium shape of an *unsupported* nanoparticle is given by the Wulff construction [16,28], a stable *supported*

nanoparticle involves an additional facet representing the free-energy per unit area of the interface with the support, as described by Winterbottom [29]. An equivalent analysis was given by Kaischew [30] and invoked by Henry [31] in an analysis of the shape of Pd particles on MgO. Properties of supported Pd_N nanoparticles have been explored in a variety of settings with an eye toward catalytic applications [32]. Clearly experimentation and modeling on a variety of catalytically active metals, on the chemically highly variable perovskite supports is desirable, in order to map out possibilities and to obtain valuable new materials.

In order to carry out first-principles studies of nanoparticle/substrate interactions and structure, it is necessary to adopt some manageable starting models. As noted above, the Winterbottom free energy construction presumably dictates which particle facets are favored for exposure and for growth atop the substrate. However, the individual free energy terms required to predict equilibrium structures are generally not known. In fact, they may be an important outcome of theoretical studies, in combination with experiment. It is hoped that high-resolution experimental data for Pt/STO will be available shortly.

Comparison of zero-dimensional (adsorbed Pd atom), two-dimensional (adsorbed Pd film) and three-dimensional (adsorbed Pd_N particle) structures enables a resolution of Pd–Pd versus Pd–support interactions and their consequences for chemical reactivity. Single atom and film models of Pd:STO are readily available; in order to make detailed comparison, typical model calculations will be reported here. Motivated by the experimental observation of 3 well-ordered structural types of palladium clusters on a STO(001) substrate [3] we have carried out periodic supercell bandstructure analyses. In addition to being well ordered, these Pd_N clusters also show preferential crystallographic orientation with respect to the substrate. These three cluster topologies can be explained by putting down a number of Pd atoms on the STO(001) surface without altering their mutual *fcc* crystal structure, named after their appearance as hexagonal (*hex*), pyramid (*pyr*), and hut (*hut*). As a classic catalyst, Pd here exposes a rich mixture of edges and surfaces, making this system very interesting in terms of modeling catalytic reactions, with a direct connection to experimental possibilities.

Both idealized SrO- and TiO_2-terminations of STO have been considered; as expected from previous studies, Pd adsorption on the TiO_2 surfaces is energetically preferred. Surface meshes consisting of (1×1), (2×1), (3×1), (2×2), (4×2) and (3×3) TiO_2 terminated surfaces have been used to support Pd clusters of varying sizes/topology; only a small subset of those models will be discussed in the following. A variety of surface reconstructions of TiO-terminated STO have been observed, depending upon preparation conditions, thermal treatment, P_{O_2}, etc. [33]. Several inequivalent models have been proposed, consistent with experiment, and questions about STO surface reconstructions and their relative stability are ongoing [34]. Before attempting to understand Pd_N particles on a reconstructed substrate, is it prudent to examine the simpler ideal atomic terminations. In any case, it is doubtful whether the previously observed and modeled reconstructed surfaces would survive the Pd – O bonding interactions upon deposition. Recent studies of sub-monolayer Pt on STO have suggested that the TiO_2 double layer termination is modified, becoming Ti-deficient [35] The basic *hex*, *pyr*, and *hut* structures seen in STM microscopy are studied here. Adsorption of several atoms (H, C and O) and small molecules (OH, CO, CH_3) on the supported Pd_N particles is modeled, to obtain some notion of their reactivity.

2. Computational methodology

The Vienna Ab Initio Simulation Package (VASP) was utilized to perform spin-restricted periodic slab DFT calculations with plane-wave basis sets [36–39]. The interactions between ionic core pseudopotentials and valence electrons were modeled using the projector augmented wave (PAW) method and corrected with the generalized gradient exchange–correlation approximation (GGA) as developed by Perdew and Wang (PW91) [5]. While PW91 and other gradient-corrected methods show systematic errors with respect to binding energy, bond lengths and magnetic properties, they are in general an improvement over LSDA alone. Hybrid-functional methods which include an empirical mix of Hartree–Fock exchange and some GGA formulation at considerable additional computational cost can offer further improvements, for example in the classic case of NiO [40]. The so-called B3LYP hybrid version has been successfully applied to study the various crystallographic phases of bulk hematite [41]. Definitive studies of particle and surface chemical reactivity may require the use of the most sophisticated methods; however, lacking an experimental basis for parametrization or choice of optimized functional, it seems best to begin with the well-tested GGA/PW91 functionals.

Grids for Brillouin zone integrations were generated automatically by the method of Monkhorst and Pack [42]. Variable *k*-point meshes were chosen for all structural relaxation, energetics and electronic property calculations such as charge and densities of states. Starting with low-order k-meshes like $3 \times 3 \times 2$, systematic extensions were made, typically up to $6 \times 6 \times 5$ to verify convergence and precision. Here and in the following the first two indices refer to the surface mesh, while the third refers to the inter-slab axis. A useful strategy for achieving rapid structural relaxation is achieved by starting with a minimal mesh, and then sequentially augmenting the mesh as geometric convergence is approached. In most cases energy convergence to better than 1 meV/cell was achieved in structural relaxations; this is well beyond any required relative comparison between models. To calculate electronic wavefunctions a plane-wave cutoff energy typically of 400 eV was used, along with the more dense k-meshes. The vacuum gap between periodic supercell slabs is typically ~15 Å. The computational methodology described above has been validated in studies of vanadium oxide and tungsten oxide on hematite surfaces [43,44].

Effective charges and atomic volumes are determined by the Bader topological analysis scheme [45], and by a spherical volume (R_{WS}) integration method. While any charge partition scheme has arbitrary elements, a comparison of Bader and R_{WS} analyses for different systems can be very useful.

A Gaussian line broadening has been used in histogram analysis of electronic densities of states (DOS); plotted lines are thus a convolution of a Gaussian of FWHM = 0.2 eV and the 'natural' linewidth due to interatomic interactions. Partial densities of states (PDOS) are determined by a combination of site-specific atomic volume integrations, with radii R_{WS}, and projections against spherical harmonics to resolve specific orbital *lm* character. Partial densities of states (PDOS) which resolve spectral contributions by different atomic types, orbital angular character, and by their spatial location provide an additional dimension by which one may understand the particle structure, and particle–adsorbate and particle–substrate interactions.

The volume-integration radii R_{WS} used are (Sr, Ti, O, Pd) = (1.56, 1.22, 1.44, 1.57) Å, taken from the Bader volume of atoms which are not adjacent to vacuum, according to $V_{bader} = (4\pi/3)R_{WS}$ [3]. Since the Bader volumes are space-filling, this choice consistently assigns electron density to atoms with little or no 'lost' interstitial volume. On the other hand, in a typical adsorption geometry, the Pd – O interatomic distance of ~2.1 Å implies a large overlap of the R_{WS} spheres, with resultant over-counting of electrons. Thus depending upon the local geometry and objectives of analysis, smaller cation radii may be preferred for analysis. Of course no physical property is affected by the choice of analysis parameters.

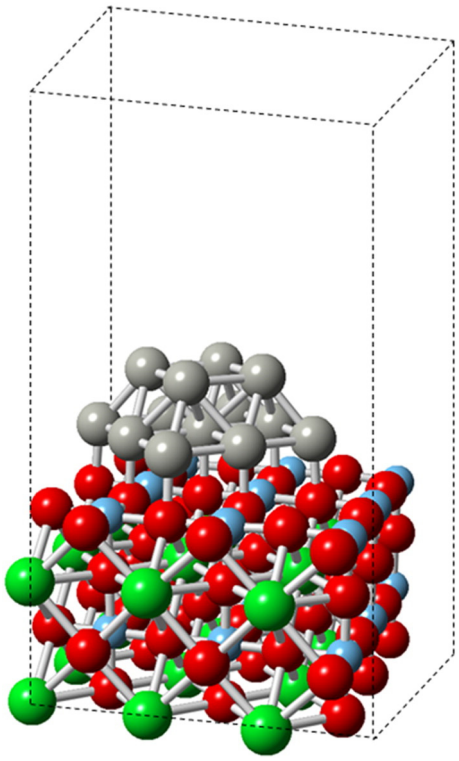

Fig. 1. Side view of STO(001) TiO_2 terminated substrate model; $3 \times 3 \times 2$ supercell with adsorbed pyr_{13} particle. Oxygen—red, titanium—blue, Sr—green, Pd—gray. (For interpretation of the references to colors in this figure legend, the reader is referred to the web version of this article.)

3. Model systems

Numerous experimental [46] and theoretical [47] studies have been made of monolayer and sub-monolayer coverages of Pd on various crystalline substrates. Adsorption of molecules [48] and oxidation [49] of Pd-deposited substrates has also been extensively reported. Since different methodologies, carried out at different times, tend to yield slightly different results, the present work aims to be internally consistent by carrying out reference calculations which can in principle be compared with previous models. Reference states consisting of isolated STO slab, a Pd atom in the interslab region, adsorbed single Pd atom and monolayer (ML) Pd on the unreconstructed oxide (001) surface will be used to calibrate the more complex nanoparticle and cluster model results. The STO(001) surface is known to exhibit a large number of surface reconstructions; e.g. (2×1), (2×2), $c(4 \times 2)$, $c(6 \times 2)$ and $c(4 \times 4)$ [32,33]. In particular the (2×1) and $c(4 \times 2)$ surfaces have been used to characterize supported Pd clusters [2]. The experiments show that clusters of the *hut* type grow on STO(001)-(2×1) while hexagonal (*hex*) and pyramidal (*pyr*) clusters grow on the $c(4 \times 2)$ reconstruction. Thus, by selection of a specific surface reconstruction it is possible to tailor the cluster topology, with specifically exposed crystallographic facets. When such tailored particles can be stabilized, very precise control of chemical and catalytic properties can be expected.

More specifically, under low deposition temperatures, the relationship between Pd *hex* axes and STO-$c(4 \times 2)$ is: Pd(111)||STO(001), Pd[110]||STO[110]. For *pyr*, also on $c(4 \times 2)$ but at high deposition temperature: Pd(001)||STO(001), Pd[100]||STO[100]. For *hut*, on STO(001)-(2×1) the Pd(011)||STO(001), Pd[110]||STO[100] alignment is observed. For free crystals/nanoparticles the relative growth rate of different facets is controlled by their free energy, as described by Wulf [6]. Winterbottom extended these considerations to growth and stability of embedded particles [7]. A truly comprehensive theory would be able to predict the relevant surface free energies; for the present, we must be content to investigate a few plausible interfaces and their energetics. In previous work combining surface diffraction data, real-space modeling, and DFT calculations a detailed atomic-resolution model of the (2×1) structure has been obtained [32]. Further experimental and theoretical studies led to a consistent picture of plausible $c(4 \times 2)$ structures and their energy ordering, based upon the addition of TiO_2 units to the TiO_2 (001) termination [50,51].

An overview of the STO(001) periodic slab structure is given in Fig. 1, showing a $3 \times 3 \times 2$ supercell used in more accurate simulations described below. Here the first two indices refer to the periodicity of the surface mesh, and the third index refers to the thickness of the slab along the c-axis direction. Minimal *hut*, *hex*, and *pyr* cluster models are shown in Fig. 2. Experience shows that 'freezing' the coordinates of a number of layers of atoms at the bottom of the slab provides adequate bulk-like boundary conditions for the relaxing surface layers and adsorbates. In the specific case of STO we find that 'rapid prototyping', in which only the topmost TiO_2 and SrO layers are allowed to relax, gives semiquantitative structural parameters and energies which can serve as initial conditions for rapidly convergent simulations with a larger number of degrees of freedom.

The binding of simple molecules like CO and hydrocarbons to Pd films and particles, and their subsequent dissociation/oxidation provides feasible models to study features of interaction and reactivity

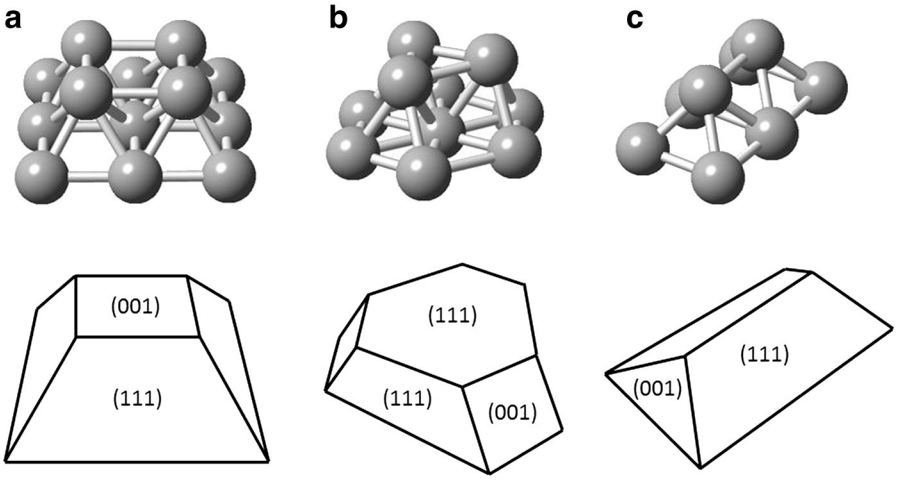

Fig. 2. Topology of Pd particles as grown on $c(4 \times 2)$ and (2×1) reconstructions of STO(001), and clusters used in DFT cluster-substrate modeling. (a) Pyramidal (b), hexagonal and (c) hut.

which can doubtless be extended to more complex systems. The combustion of methane over Pd/PdO catalysts has been studied experimentally, and is considered to be a complex process, depending upon temperature and concentration of various reactants and products [52]. The oxidative insertion of a single Pd atom into the CH bond of methane has been examined theoretically by De Jong et al. [53]. Activation of methane on a Pd_3 particle has been modeled using DFT [54]. Dissociation and photodissociation of CH_4 on Pd(111) has also been calculated by DFT methods [55], and recent studies have emphasized the so-called 'active phase' of methane on Pd(111) and PdO(101) during methane oxidation [56]. A thorough study of even a basic reaction like $CH_4 \rightarrow CH_3 + H$ on Pd_N would involve tracing a number of initial states through adsorption trajectories, to final state exit trajectories. In the present work we will be content to examine a few plausible initial, intermediate, and final state scenarios in a static framework.

4. Results

4.1. Structure and electronic properties of supported Pd

Being well aware of the many observed reconstructions of STO(001) surfaces, we nevertheless think it very useful to explore the topologically simple ideal bulk-cleavage surfaces to gain information about chemical and structural tendencies of adsorbates. Cohesive energies of particles, adsorbed atoms and molecules are calculated self-consistently, and reported below relative to appropriate 'reference states'; for 'isolated adsorbate' we typically use a model with the adsorbate in the mid-gap region between relaxed substrate slabs. These reference energies are of course strictly not the energies of truly isolated species; however, this procedure permits the precise determination of energies of adsorption largely free of errors induced by differing boundary conditions. From a physical point of view the resulting *adhesion energy* may be considered as the work necessary to separate the adsorbate from its support. This is useful to consider surface binding separately from the structural relaxation. Necessity of a common Fermi energy in self-consistent DFT, even for well separated systems, generally leads to a charged ion/particle in the interslab region. In order to relate such artificial states to a common reference, such as the neutral atom in a box, some additional atom/ion-in-box calculations are occasionally useful. In the following, any such shift in reference states is clearly identified.

4.1.1. Adsorbed Pd atoms and films up to 2 ML

The first model considered consists of a periodic slab with dimensions of $1 \times 1 \times 2$ unit cells in the x-, y-, and z-directions respectively. In the [001] or c-axis direction the stacking sequence is TiO_2–SrO–TiO_2–SrO with a vacuum gap between slabs of ~15 Å, permitting studies of adsorption on either TiO_2 or SrO faces. Previous variational calculations on STO slabs show that relaxing only two terminal layers is sufficient to capture the main structural features, and permits the rapid survey of a considerable number of models. As verification of this procedure is critical for assuring the precision of calculated adsorption in more complex systems, a fairly detailed analysis is given here. The results found for adsorbed atoms and films form a 'baseline' necessary for understanding differences due to presence of facets, edges and vertices in more complex geometries. A uniform computational procedure and logical thread for all systems studied here is thus established. For highly precise energetic determinations a thicker slab with a greater number of degrees of freedom would be required. Simulations carried out with larger surface meshes and thicker slabs, vide infra, show that the main structural features and relative energetics are already captured in this minimal model, which is referred to in the following as $(1 \times 1 \times 2)$. The relevant O-*atop*, O-*hollow*, O-*bridging* and Ti-*atop* sites are shown in Fig. 3.

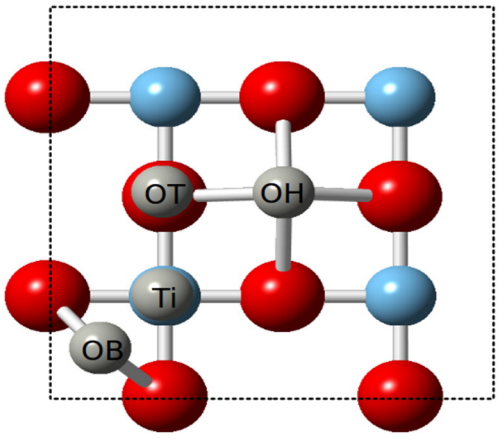

Fig. 3. Top view of TiO_2 terminated STO(001), showing idealized O-*atop* (OT), O-*hollow* (OH), Ti-*atop* (Ti) and O-*bridge* (OB) ad-atom sites.

Placing one Pd atom on this cell corresponds to 1/2 monolayer (ML) coverage; i.e. one of the two surface oxygens is bonded to Pd. Table 1 shows relative energetics of different geometries (1/2-, 1- and 2 ML), for adsorption on the TiO_2 surface; higher energy sites found on the SrO termination are not reported here. The reference state used here consists of the STO slab plus the surface-relaxed Pd film placed at mid-gap, resulting in the so-called *work of adhesion*. Relative energies are of course independent of the chosen reference state. The Pd *atop* O configuration, at 1.15 eV/Pd is favored by 0.08 eV over the O – O *bridge* site; other sites are considerably less stable. The rather strong Pd – Pd binding leads to increased energy of $1.15 < 2.05 < 2.74$ eV/Pd for 1/2-, 1-, and 2-ML coverages respectively. Recall that for 1 ML every surface O is bonded to a Pd; this is twice the Ti surface concentration. The corresponding vertical displacements above the ideal TiO_2 plane are $\Delta z = 2.24$ and 2.23 Å for 1- and 2-ML; in the latter case, the second overlayer is found at 4.26 Å. The corresponding Pd – O bond lengths are 2.23 and 2.22 Å respectively. In the 2 ML case, the predicted Pd – Pd distance is 2.76 Å, compared with 2.80 Å for bulk Pd.

The R_{WS} volume charges and Q_B Bader charges reveal a rather stable electronic configuration for the surface layers, with a tendency toward greater charge transfer from Pd to O with increasing coverage. Thus, Q_B(Pd) ranges from −0.21 to +0.24 e in the 2-ML coverage. The Pd PDOS for 1/8 ML coverage at different binding sites, compared with "free" Pd in the slab-gap, are given in Fig. 4a. In Fig. 4b we see the effects of Pd – O bonding on the surface layer oxygens. With increased coverage the Pd PDOS for 2 ML (not shown) reveals an extended occupied conduction band width of ~6 eV, with some significant differences seen between the Pd – O contact layer and the Pd – Pd overlayer. In particular, the top layer distribution is more narrow, with a sharper peak around the Fermi energy E_F.

Following the notation developed above, we next describe an expanded $(2 \times 2 \times 2)$ periodic slab; i.e. of size two unit cells in all three dimensions. Positioning one Pd atom per cell on the surface corresponds to 1/8 ML coverage; 1/8-, 1/4-, 1/2- and 1-ML coverage sites on the TiO_2 termination are reported in Table 2; higher energy SrO-terminated sites are not listed. Monotonic increase of binding with Pd coverage is again found: $1.48 < 1.69 < 1.98 < 2.53$ eV/Pd respectively for the close-packed or particle configurations, which are greater than or equal to those of dispersed geometries. The corresponding Δz vertical coordinates are $2.04 < 2.08 < 2.10 < 2.19$ Å respectively, with Pd – O bond lengths of $2.05 < 2.08 < 2.11$–$2.15 < 2.22$ Å. The calculated difference in energy (0.5 eV/Pd) and Pd – O bond (0.05 Å) between $1 \times 1 \times 2$ and $2 \times 2 \times 2$ 1 ML Pd models can be attributed to Pd–Pd interactions in the finite slab environment. Such model-dependent energy shifts have no effect upon relative energy comparisons within a single surface model.

Table 1
Properties of supported Pd in 1/2-, 1-, and 2-ML coverages on ideal TiO_2 terminated STO(001) in minimal 1 × 1 × 2 supercell model.

1 × 1 × 2 supercell	Energy/Pd	Bond length	Bader charge	R_{WS} charge
1/2 ML	1.15	Pd–O 2.08	Sr +1.53, 1.55	+1.96, 2.02
Pd *atop* O		–Ti 2.84	Ti +2.06, 2.14	+2.19, 2.20
		–Pd 3.91	O −1.09, −1.31	−0.92, −1.26
			Pd +0.01	+0.86
O *bridge*	1.07	Pd–O 2.32	Sr +1.54, 1.56	+1.97, 2.02
			Ti +2.03, 2.13	+2.13, 2.20
			O −1.14, −1.31	−0.92, −1.21
			Pd +0.06	+0.91
O *hollow*	0.8	Pd–O 2.56	Sr +1.53, 1.55	+1.96, 2.02
			Ti +2.08, 2.13	+2.18
			O −1.21, −1.31	−0.92, −1.26
			Pd +0.16	+1.00
atop Ti	0.54	Pd–Ti 2.44	Sr +1.53, 1.57	+1.96, 2.02
			Ti_1 +2.02	+2.15
			O_1 −1.14	−0.92, −1.16
			Pd +0.03	+0.99
1 ML	2.05	Pd–O 2.23	Sr +1.54, 1.57	+1.96, 2.02
Pd @ (0, 1/2), (1/2, 0)		–Ti 2.94	Ti +2.04, 2.13	+2.19, 2.20
		–Pd 2.76	O −1.14, −1,30	−0.92, −1.18
			Pd −0.12, +0.14	+0.77
2 ML	2.74	Pd–O 2.22	Sr +1.54, 1.57	+1.97, 2.02
Pd @ (0, 1/2), (1/2, 0),		–Ti 2.94	Ti +2.06, 2.13	+2.18, 2.20
(0, 0), (1/2, 1/2)		–Pd 2.76	O_x −1.15, −1.31	−0.92, −1.19
			Pd −0.21, +0.24	+0.74

Binding energy (eV/Pd) is given relative to the same Pd_N structure placed at mid-gap between STO slabs. Bond lengths are given in Å. Bader charge and R_{WS} charge (e) as described in the text; R_{WS} (Sr, Ti, O, Pd) = (1.57, 1.21, 1.44, 1.56 Å).

Charge analyses for Pd in different geometries are also presented in Table 2. Trends identified in the minimal 1 × 1 × 2 model are here verified: stable surface electronic configurations, and increasing Pd → O charge transfer with increasing coverage. In the 1/8 ML coverage the Pd Bader charge is 0.05 e and the volume integrated R_{WS} charge is 0.80 e. Both measures indicate an expected charge transfer from metal to oxygen; the absolute values are small compared to nominal values (e.g. Pd^{+2}, O^{-2}). Q_B(Pd) is −0.04 to +0.02 e for 1/2 ML and ranges from −0.12 to +0.13 e for 1 ML coverage; positive Pd charge is generally associated with close proximity to oxygen.

The PDOS for 1/8 ML Pd at different adsorption sites for TiO_2 terminated STO(001) (not shown) reveal immediately that the high binding energy *atop* and *bridge* sites (relative to surface oxygen) produce a large and characteristic deformation of the Pd levels, due to their bonding interaction with the substrate oxygen. Parenthetically, we note the small feature above E_F in the 'free atom' spectrum, showing the weak Pd–Pd interaction in the periodic-box reference state.

A further expanded 3 × 3 surface cell was used to model supported particles as reported in the following. This supercell allows for some greater separation between periodic Pd_N particles.

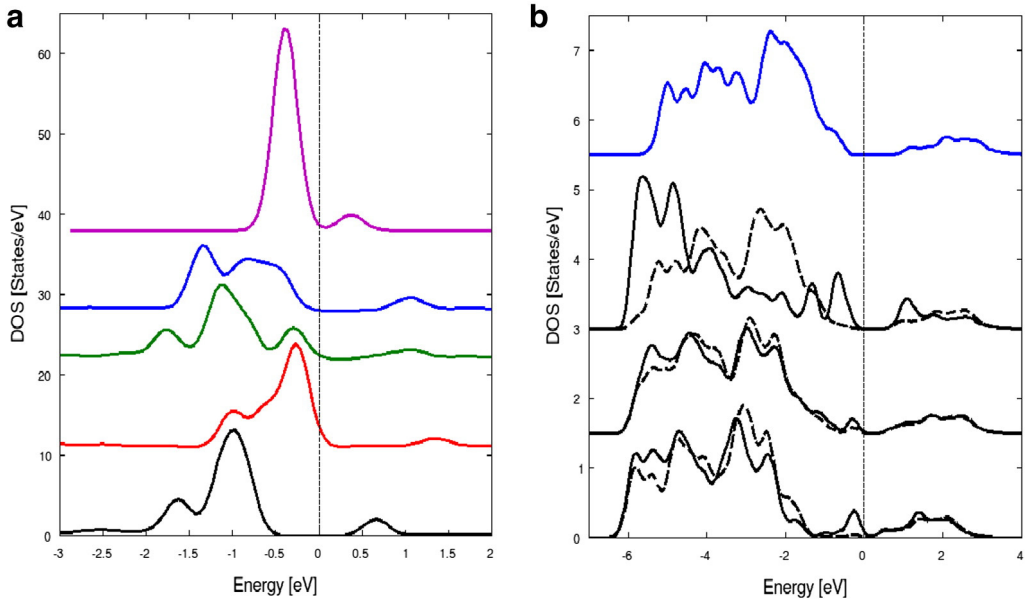

Fig. 4. (a) PDOS for single Pd atom adsorbed on 2 × 2 TiO_2 termination, at different sites. From top: Free = magenta, O-*atop* = blue, O-*bridge* = green, O-*hollow* = red, Ti-*atop* = black. (b) PDOS for surface oxygen with Pd atom adsorbed on 2 × 2 TiO_2 termination, at different sites. From top: (i) no Pd, (ii) Pd-*atop*, (iii) Pd-*bridge*, (iv) Pd-*hollow*. Solid black line is Pd–O bond; dashed line for other oxygens. DOS curves are normalized with respect to number of oxygen atoms. (For interpretation of the references to colors in this figure legend, the reader is referred to the web version of this article.)

Table 2
Cohesive energy (eV/Pd) of Pd_N adsorbates is given relative to Pd_N placed in mid-gap between STO slabs. Bond distances are given in Å, using STO(001) 2 × 2 × 2 and 3 × 3 × 2 supercell models. Fractional coordinates (*h*, *k*) are given for overlayers. Positive energy denotes net binding. Positive Pd Bader charge and volume integrated R_{WS} charge (e) show electron transfer away from Pd sites; negative charge shows electron accumulation. R_{WS} (Sr, Ti, O, Pd) are (1.57, 1.21, 1.44, 1.56 Å). Multiple charge values indicate range found.

2 × 2 × 2 supercell	Energy/Pd	Bond distance	Bader charge	R_{WS} charge
1/8 ML	1.48	Pd – O 2.05	Pd 0.05	0.8
Pd *atop* O				
O *bridge*	1.47	Pd – O 2.28	Pd 0.12	0.85
O *hollow*	1.22	Pd – O 2.48	Pd 0.18	0.94
atop Ti	0.88	Pd – Ti 2.39	Pd 0.11	0.96
1/4 ML	1.55	Pd – O 2.08	Sr +1.53, 1.55	+1.96, 2.12
Pd @ (1/2,1/4) (0,3/4)		– Ti 2.85	Ti +2.10, 2.14	+2.20
dispersed		– Pd 5.52	O −1.07, −1.30	−0.92, −1.14
			Pd −0.03	+0.82
Pd @ (1/4, 0) (0,1/4)	1.69	Pd – O 2.07	Sr +1.53, 1.56	+1.95, 2.02
compact		– Ti 2.85–2.89	Ti +2.02, 2.17	+2.18, 2.20
		– Pd 2.78	O −1.11, −1.31	−0.92, −1.23
			Pd −0.04, +0.04	+0.78
1/2 ML	1.62	Pd – O 2.08	Sr +1.56, 1.58	+1.96, 2.02
Pd_4 dispersed		– Ti 2.81–2.84	Ti +2.04, 2.17	+2.19, 2.20
		– Pd 3.91	O −1.12, −1.32	−0.92, −1.26
			Pd −0.16, +0.19	+0.86
Pd_4 ribbon	1.98	Pd – O 2.14–2.15	Sr +1.53, 1.56	+1.96, 2.02
compact		– Ti 2.81–2.95	Ti +2.04, 2.14	+2.18, 2.20
		– Pd 2.77–2.78	O −1.12, −1.30	−0.92, −1.23
			Pd −0.04, +0.02	+0.78, 0.81
1 ML	2.53	Pd – O 2.22	Sr +1.53, 1.59	+1.96, 2.12
Pd_8 *atop* O		– Ti 2.93–2.94	Ti +2.04, 2.13	+2.19
		– Pd 2.76	O −1.15, −1.30	−0.92, −1.19
			Pd −0.12, +0.13	+0.77
pyr_5	2.35	Pd – O 2.14	Sr +1.53–1.55	+1.96, 2.02
in registry with O		– Ti 2.79	Ti 1.98–2.13	+2.17, 2.20
		– Pd 2.65–2.67	O −1.16, −1.30	−0.92, −1.26
			Pd −0.28, +0.19	+0.70, +0.78
3 × 3 × 2 supercell				
pyr_5	2.89	Pd – O 2.08	Sr +1.54	+2.02, 2.03
		– Ti 2.82	Ti +2.00, 2.12	+2.18, 2.24
		– Pd 2.69–2.70	O −1.17, −1.29	−0.90, −1.23
			Pd −0.14, +0.06	+0.69, +0.78
pyr_{13}	2.64	Pd – O 2.13–2.25	Sr +1.54, 1.55	+1.96, 2.02
		– Ti 2.80–2.87	Ti +2.01, 2.22	+2.17, 2.20
		– Pd 2.64–2.79	O −1.11, −1.31	−0.92, −1.23
			Pd −0.14, +0.12	+0.53, +0.77
$flat_{13}$	2.18	Pd – O 2.10	Sr +1.53, 1.60	+1.96, 2.02
		– Ti 2.87	Ti +2.07, 2.15	+2.17, 2.21
		– Pd 2.69–2.87	O −1.10, −1.31	−0.93, −1.26
			Pd −0.01, +0.05	+0.69, +0.82
pyr_{14}	2.66	Pd – O 2.16–2.21	Sr +1.54,1.58	+1.95,2.02
		– Ti 2.84–2.98	Ti +2.05, 2.19	+2.17, 2.20
		– Pd 2.63–2.81	O −1.11, −1.31	−0.92, −1.24
			Pd −0.12, +0.13	+0.55, +0.78
hex_{10}	2.52	Pd – O 2.13–2.22	Sr +1.54, 1.58	+1.94, 2.02
		– Ti 2.62	Ti +1.97, 2.15	+2.16, 2.20
		– Pd 2.62–2.73	O −1.14, −1.31	−0.92, −1.19
			Pd −0.10, +0.11	+0.52, +0.80
hut_8	2.43	Pd – O 2.16–2.21	Sr +1.54, 1.58	+1.94, 2.12
		– Ti 2.58–2.68	Ti +2.01, 2.14	+2.16, 2.22
		– Pd 2.65–2.75	O −1.11, −1.32	−0.92, −1.21
			Pd −0.17, +0.15	+0.64, +0.77

4.1.2. Supported Pd_N particles

The minimal model of *pyr* symmetry has five Pd atoms with a 4-fold base which sits in good registry atop substrate oxygen (Table 2); only (111) facets are available. The next larger sizes studied here have 13 or 14 metal atoms (Fig. 1), presenting (111) and (100) facets with a greater variety of edges and vertices exposed to participate in adsorbate interactions. The minimal cluster model of *hex* symmetry has ten Pd atoms, while *hut* has eight; see Fig. 2. After some experimentation with 2 × 2 × n and 3 × 1 × n surface supercells, a 3 × 3 × 1 model was selected as a compromise between the desire to keep particles and their adsorbates well separated, and computational time required for structural relaxation. In each of the particles described below the initial Pd – Pd distances were taken as 2.761 Å as in Pd metal. One might well ask whether such small particles are relevant to experimental properties of larger particles of say, 10–20 nm size which are frequently imaged. Nanoparticles of whatever size presumably nucleate as very small particles which grow, so the presently studied objects must have considerable importance, even if they are difficult to observe. The chemical reactivity of key facets, edges and vertices characteristic of a particular topology can be described within the limitations mentioned above. Furthermore, 'real nanoparticles' may be expected to display defects such as vacancies, dislocations, steps and twinning which would require a larger length scale of simulation, beyond simply using larger idealized particles. In any case, small (4–8 atom) particles are known to be highly effective in well-dispersed catalysts, with the support playing an important role in suppressing diffusion and particle agglomeration.

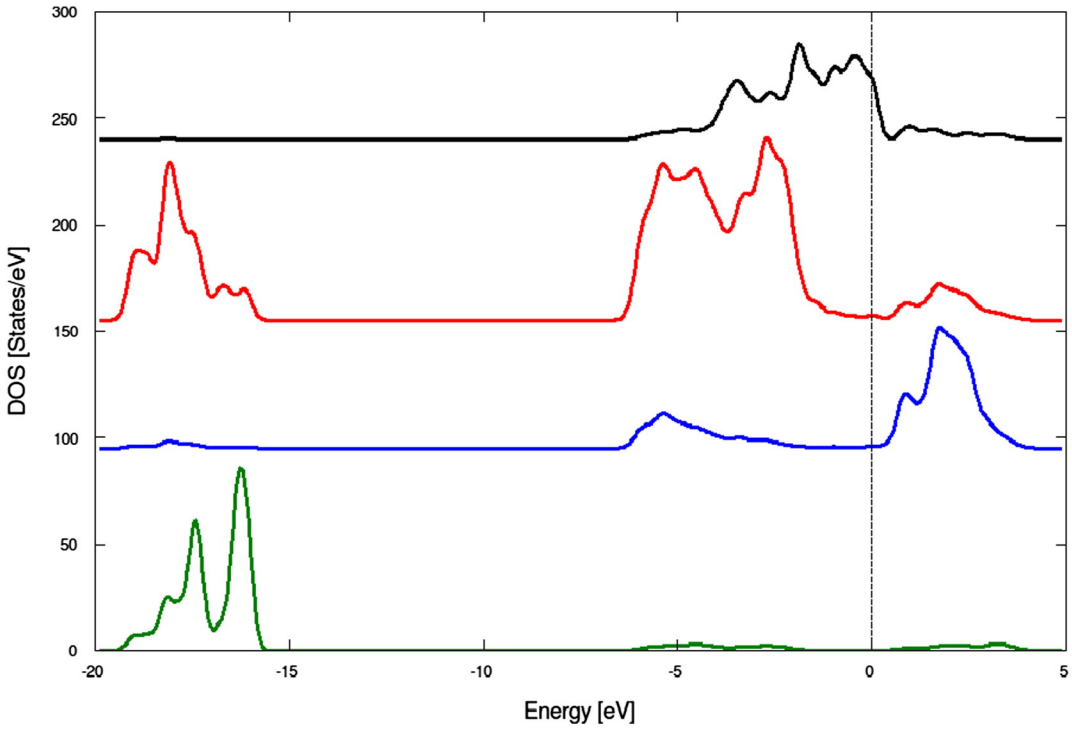

Fig. 5. Atom resolved PDOS of pyr_{13} cluster adsorbed on TiO_2 terminated STO(001) 3×3 slab. From top: Pd (black), oxygen (red), Ti (blue) and Sr (green). DOS curves are not normalized with respect to number of atoms. (For interpretation of the references to colors in this figure legend, the reader is referred to the web version of this article.)

In the initial $2 \times 2 \times 2$ model of pyr_5 the cohesive energy per Pd atom is 2.35 eV, compared to 2.89 eV with a $3 \times 3 \times 2$ surface mesh, see Table 2. The Δz Pd heights relative to the oxygen basal plane are (2.16, 4.06) Å in 2×2 vs (2.09, 4.01) Å in 3×3 models. The corresponding Pd – O and Pd – Pd bond lengths are (2.08, 2.69–2.70) Å and (2.13–2.25, 2.64–2.79) Å respectively. The difference in energy of ~0.5 eV/Pd

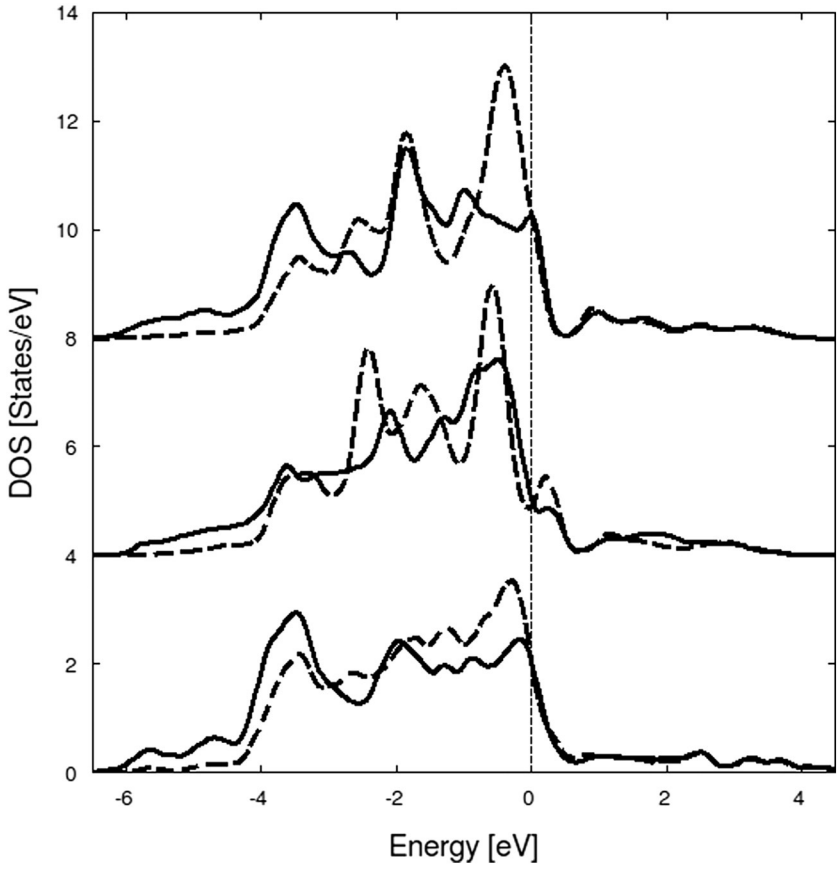

Fig. 6. Layer-resolved Pd PDOS for (a) pyr_{13}, (b) hex_{10}, (c) 2 ML film. Contact layer—solid line, 2nd layer—dashed line. DOS curves are normalized with respect to number of Pd atoms.

and in structural parameters can be attributed to the interparticle interaction in the smaller mesh, where the center to center distance is 7.83 Å. These interparticle interactions are of importance in the tendency to particle agglomeration at high temperatures observed on catalyst supports. As an aside, we note that an energy of 2.92 eV/Pd is found for a $3 \times 3 \times 1$ surface model, showing the relative unimportance of slab-thickness effects.

The nine base-plane metal atoms of pyr_{13} are in very good registry to O-*atop* positioning. The Pd – Pd nearest neighbor distances in the contact layer lie between 2.64 and 2.69 Å, to be compared with 2.75 Å for a Pd(001) surface, consistent with free particle vs solid differences. The partial densities of states of a pyr_{13} cluster adsorbed on TiO_2 terminated STO(001) in the $3 \times 3 \times 2$ model are given in Fig. 5. From this figure one sees the strong overlap of Pd *4d* states with the oxygen upper valence band (UVB) and a significant admixture of Ti *3d* states into the bottom region of this band. The overlap between Pd and Ti states is relatively small, the Ti UVB feature being a well-known indicator of Ti – O covalency and deviation from the nominal Ti^{4+} $d^0s^0p^0$ cation state. The occupied portion of the oxygen UVB, ~7 eV in width, shows two well-defined sub-bands which can be roughly identified with (t, e) quasi-octahedral crystal field states. The lower valence band (LVB), from ~16 to 19 eV, is dominated by O 2 s states, and by the Sr 4 *s–p* bands. The energy overlap of oxygen and Sr states does not necessarily indicate a strong covalency; examination of the electron densities in the interatomic region verifies an essentially ionic bond as is conventionally assumed. A small but non-negligible Ti participation in the LVB is visible, as an indication of the hybridized *s–p–d* Ti – O bonding interaction. The low-lying conduction states are dominated by Ti *3d* and antibonding O states, as expected. A smaller, but significant Pd excited state density is also present, and will be highly involved in chemisorption processes. The Sr excited state density is negligible.

In Fig. 6 are given height-resolved PDOS for clusters pyr_{13} and hex_{10} and for a 2 ML film. PDOS curves are normalized with respect to the number of atoms in each layer; i.e., (9, 4) and (7, 3) respectively. From these data we can extract some information about particle–substrate interactions, and variations between different particle topologies. First, concerning the *pyr* cluster, one sees that the 9-atom layer in contact with STO has a broadened structure of width of ~6 eV with considerable intensity shifted below E_F. The upper 4-fold structure exhibits narrower bands, with a strong peak just below E_F which will dominate the Pd_{13} surface activity. The *pyr* PDOS is thus *very* different from that of the isolated adsorbed Pd, by comparison with Fig. 4. The excited state structure is identical for the two 'layers' of the particle. Next, concerning the hex_{10} adsorbed particle, Fig. 6b, one sees gross similarities to that of *pyr*: band width of ~6 eV and more narrow and sharply peaked structures near E_F for the top layer. In detail several structure-dependent differences are apparent, including a triple-peaked top layer occupied state region, and a bi-layer low intensity peak just above E_F which would differentiate the *pyr* and *hex* interactions with incoming atoms/molecules.

A hex_{10} particle was chosen as a minimal model of hexagonal symmetry nanoparticles; here (100) and (111) facets are revealed (see Figs. 2, 7) but $(111,111)^*$ edges and $(111, 111, 100)^+$ corners are not represented. Distorted registry of the seven metal atoms in contact with oxygen of the STO(001) substrate is accommodated with several Pd in a O – O *bridge* configuration. The binding energy of 2.52 eV/Pd is substantial, but less than that of the near-perfect registry pyramidal particles. The Pd – Pd nearest neighbor distances in the contact layer are between 2.62 and 2.95 Å to be compared with 2.75 Å for the Pd(111) surface. The 7 contact layer atoms are quite planar, ranging from 2.025 to 2.125 Å above the surface O-plane. A better hex_{21} representation containing all edges and corners can be formed, which would imply a larger surface mesh, e.g. $(4 \times 4 \times 2)$ with 160 atoms/cell, which was not undertaken here.

The hut_8 cluster (Fig. 7c) exhibits the minimal features of the elongated structure, showing (100) and (111) facets, and all required edges and corners. Initial Pd – Pd bond lengths of 3.89 Å and 2.75 Å (short/long side of *hut*) were taken from the Pd(011) surface, but then relaxed on the substrate. However when the structure relaxes Pd – Pd distances change considerably and it is clear that a small *hut* cluster cannot stabilize in the same way as *pyr* and *hex* on a small surface-mesh TiO_2 terminated unreconstructed STO(001). Recall that experimentally, *hut* is seen on (2×1) surface reconstructions while *hex* and *pyr* are seen on $c(4 \times 2)$ surfaces.

Relative energies of sites and charge distributions on the TiO_2 termination of STO(001) are reported in Table 2. It is immediately apparent that Pd–Pd interactions favor cluster formation over that of a flat film on STO(001). The quite small energy difference of *hut* vs film is (0.03 eV/Pd) which is a further indication of the relative instability of the minimal-sized particle.

4.2. Atomic adsorption on zero-, two- and three-dimensional Pd

Now we turn to study atomic adsorption, as a probe of chemical reactivity which depends upon the metal electronic states as modulated by the Pd–substrate interaction and the topology of the interacting Pd_N metallic structure. Here H, C and O adsorption on supported Pd is modeled to gain a measure of chemical reactivity of the metal species. The notation O^* will be used as necessary to differentiate adsorbed from substrate oxygen in the following.

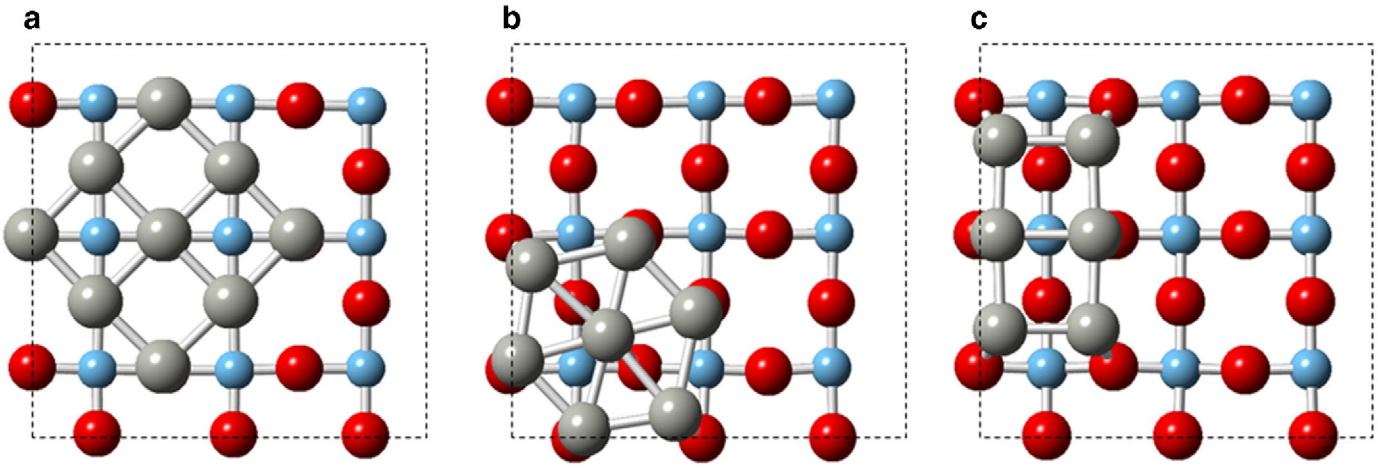

Fig. 7. Top view of interface for relaxed Pd particles on a 3×3 STO(001) substrate. (a) pyr_{13} Pd(001)||STO(001), Pd[100]||STO[100]. (b) hex_{10} Pd(111)||STO(001), Pd[110]||STO[110]. (c) hut_8 Pd(011)||STO(001), Pd[110]||STO[100]. Only interface atoms are shown. Unit surface mesh indicated by dotted lines.

4.2.1. 0-D atomic adsorption

The calculated binding energies of H, C and O in the *atop*-Pd geometry in the 1/8 ML coverage 2 × 2 model are (3.78, 4.61, 3.73) eV respectively, shown in Table 3. The corresponding Pd – X bond lengths (1.56 < 1.76 < 1.81 Å) are also reported in the table, showing the expected increase with ligand atomic radius. The Pd – O metal–substrate bond lengths are noticeably modified by atomic adsorption (2.14 < 2.27 > 2.16 Å) for the lowest-energy (atop, bridge, bridge) H, C and O adsorption sites. These values may be compared with the calculated Pd – O distances of (2.05 < 2.08 = 2.08 < 2.22 = 2.22 Å) for 1/8, 1/4, 1/2, 1 and 2 ML Pd coverages in the same Pd:STO slab model. This is not surprising, in view of the redistribution of metal–ligand bonding in the adsorption process.

Atomic charges calculated in the Bader topological scheme show a progressive charge transfer from Pd to ligand: (0.11 < 0.29 < 0.61 e) for H, C, and O respectively. The corresponding charge accumulation on the adsorbate atom is (−0.09, −0.16, −0.69 e).

4.2.2. 2-D atomic adsorption onto supported Pd films

Within the 2 × 2 surface model atomic adsorption on 1 ML Pd is reported in Table 3. One sees that for O the most favorable adsorption site is, as in 1/8 ML, Pd – Pd *bridge* where the atom can form two Pd – O bonds, with binding energy of 5.10 eV. Able to form only a single Pd – H bond, H favors the *atop* site by ~0.5 eV. Carbon favors the multiply bonded 4-fold Pd-*hollow* site with an advantage of more than 3 eV compared to the *atop* site, while the 2-fold *bridge* site is unstable, relaxing into the *hollow*. The corresponding Pd – X bond lengths increase (1.61 <1.97 < 1.98 Å), as would be expected in the shared-bond environment. The adsorption energies given in Table 3 are all relative to a reference state consisting of non-spin polarized atoms placed at mid-gap of the slab supercell. The absence of spin polarization and a non-zero atomic charge in the reference state, lead to larger 'adsorption energies' than would be found with the traditional spin-polarized isolated atom reference. For purposes of later comparison with molecules and particles and for cancelation of systematic (box size, energy cutoff, k-

Table 3
Atom and molecule adsorption on supported Pd atoms on TiO_2 terminated STO(100) in the 2 × 2 × 2 substrate model. Pd site relative to surface oxygen, corresponding to 1/8- and 1-ML coverage; adsorbate coverage corresponds to 1/8 ML. Binding energies (eV) are given with respect to atom/relaxed molecule located at mid-gap between STO slabs with identical computational parameters. Pd – X bond lengths are given in Å; Bader charges are given in e.

1/8 ML							
Adsorbate	H	C	O	CO	OH	CH_3	CH_3+H @ O
atop O: energy	3.78	4.61	3.73	2.48	2.13	2.31	0.71
Pd – X	1.58	1.76	1.81	1.85	1.91	2.03	Pd – C 2.03
– O	2.14	2.09	2.00	2.05	1.98	2.14	– O 2.14
				C – O* 1.16	O* – H 0.96	C – H 1.10	C – H 1.10
							O – H 1.00
Q_B	Pd +0.15	Pd +0.27	Pd +0.55	Pd +0.26	Pd +0.55	Pd +0.33	Pd −0.12
	H −0.17	C −0.18	O* −0.59	C +1.81	O* −1.54	C −1.31	C −0.19
				O* −2.05	H +1.00	H +0.01, +0.02	H −0.01, +0.01
O – O *bridge*: Energy	2.71	4.79	3.79	2.41	2.42	2.37	3.14
Pd – X	1.56	1.75	1.82	1.85	1.98	2.03	Pd – C 2.03
– O	2.35	2.27	2.16	2.31	2.22	2.17	– H 1.00
				C – O* 1.17	O* – H 0.98	C – H 1.10,1.11	– O 2.17
							C – H 1.10,1.14
Q_B	Pd +0.11	Pd +0.29	Pd +0.61	Pd +0.21	Pd +0.42	Pd +0.22	Pd +0.07
	H −0.09	C −0.16	O* −0.69	C +1.68	O* −1.46	C −0.15	C −0.03
				O* −1.91	H +1.00	H −0.06, +0.01	H 0.0, +0.03
1-ML							
Adsorbate/site	H	C	O	CO	OH	CH_3	CH_3+H
top Pd: Energy	4.16	5.39	4.44	2.08	3.08	2.91	5.80 Dissociated
Pd – X	1.61	1.75	1.82	1.85	1.95	2.02	Pd – C 2.03
– O	2.08–2.24	2.13–2.26	2.16–2.24	2.20–2.31	2.10–2.27	2.19–2.24	– O 2.19–2.40
				C – O* 1.16	O* – H 0.98	C – H 1.10	O – H 1.06
							C – H 1.10
Q_B	Pd −0.05, +0.06	Pd −0.05, +0.13	Pd −0.03, +0.34	Pd −0.05, +0.16	Pd +0.01, +0.27	Pd −0.06, +0.22	Pd −0.19, +0.13
	H −0.05	C −0.08	O −0.63	C +1.81	O* −1.43	C −0.27	C −0.37
				O* −1.91	H 0.00	H +0.01, +0.14	H +0.04, +1.00
Pd_2 *bridge* Energy	3.67	9.15 relaxes to 4-fold	5.1	2.45	3.25	2.76	4.12 dissociated
Pd – X	1.66, 1.82	1.97	1.98	1.99, 2.00	2.12	2.04	Pd – C 1.07–1.86
– O	2.14–2.23	2.11–2.12	2.17–2.23	2.17–2.24	2.12–2.30	2.14–2.25	– O 2.15–2.39
				C – O* 1.18	O* – H 0.98	C – H 1.10–1.16	– H 0.56–1.07
							C – H 1.07–1.11
Q_B	Pd −0.06, +0.06	Pd −0.05, +0.09	Pd −0.00, +0.30	Pd −0.07, +0.11	Pd −0.06, +0.24	Pd −0.02, +0.13	Pd −0.21, +0.82
	H −0.11	C −0.37	O −0.70	C +1.66	O −1.44	C −0.10	C −0.06
				O −1.87	H 0.00	H −0.04, +0.02	H −0.08, +0.08
Pd_4 *hollow* Energy	3.4	8.71	4.98	2.04	2.87	2.78	6.42
Pd – X	>3	1.97	2.20	2.21	2.20	2.02	Pd – C 1.09
– O	2.17–2.32	2.16–2.17	2.18–2.29	2.16–2.42	2.18–2.29	2.22–2.26	– O 2.15–2.38
				C – O 1.20	O – H 0.96	C – H 1.10–1.12	C – H 1.09–1.14
Q_B	Pd −0.07, +0.10	Pd −0.06, +0.14	Pd −0.02, +0.23	Pd −0.10, +0.13	Pd −0.10, +0.25	Pd −0.02, +0.10	Pd −0.08, +0.08
	H −0.11	C −0.48	O −0.77	C +1.63	O −1.52	C −0.13	C −0.18
				O −1.97	H 0.00	H −0.02, +0.01	H +0.03, +0.07

Table 4
Atom and molecule adsorption on supported pyr_5 and pyr_{13} clusters on TiO_2 terminated STO(100) in 3 × 3 × 1 substrate model. Pd pyramidal base is in registry to surface layer oxygen; adsorbate/molecular coverage corresponds to 1/9 ML; see text. Binding energies (eV) are given with respect to atom/relaxed molecule located at mid-gap between STO slabs with identical computational parameters. Pd – X bond lengths are given in Å. Bader charges are given in e units. Site code: *top–top* (*tt*), top–*bridge* (*tb*), top–*hollow* (*th*), *side-bridge-outer* (*sbo*), *side-bridge-inner* (*sbi*), *side-low-inner* (*sli*), *side-hollow-outer* (*sho*), *side-hollow-inner* (*shi*), *side-high-edge* (*she*), *side-bridge-high* (*sbh*).

pyr_5							
Adsorbate	H	C	O	CO	OH	CH_3	CH_3+H @ O
top Pd Energy	2.61	4.8	3.5	1.14	7.71	2.25	0.01
Pd – X	Pd – O 2.13 – H 1.56	Pd – O 2.20 – C 1.71	Pd – O 2.15 – O 1.78	Pd – O 2.16 – C 1.89 C – O* 1.16	Pd – O 2.14 – O 1.95 O* – H 0.97	Pd – O 2.13 – C 2.01 C – H 1.10	Pd – O 2.13 – C >3 – H 1.56 C – H 1.09
Q_B	Pd −0.02, +0.15 H −0.11	Pd −0.03, +0.07 C −0.10	Pd +0.04, +0.18 O −0.70	Pd +0.02, +0.11 C +1.57 O* −1.85	Pd +0.04, +0.21 O* −1.58 H +1.00	Pd −0.10, +0.14 C −0.21 H +0.05	Pd −0.11, +0.16 C +0.18 H −0.07, −0.03
Pd_2 *bridge* Energy	3.19	6.86	4.65	1.92	8.62	2.35	−0.19
Pd – X	Pd – O 2.14–2.15 – H 1.65, 1.73	Pd – O 2.16–2.25 – C 1.83, 1.84	Pd – O 2.15–2.19 – O 1.92, 1.93	Pd – O 2.15–2.19 – C 1.93, 1.96 C – O* 1.19	Pd – O 2.14–2.21 – O* 2.04, 2.12 O* – H 0.97	Pd – O 2.14–2.15 – C 2.05 C – H 1.10,1.13	Pd – O 2.14–2.15 – C 2.05, 2.35 – H 1.25 C – H 1.10, 1.13
Q_B	Pd −0.09, +0.07 H −0.09	Pd −0.02, +0.29 C −0.26	Pd +0.01, +0.25 O −0.79	Pd +0.02, +0.25 C +1.61 O* −1.89	Pd +0.01, +0.35 O* −1.58 H +1.00	Pd −0.05, +0.18 C −0.27 H 0.00, +0.07	Pd +0.03, +0.17 C −0.26 H −0.09,+0.06
Pd_3 *hollow* Energy	3.25	7.31	4.43	2.01	8.18	2.07	−0.83
Pd – X	Pd – O 2.13–2.19 – H 1.73,1.83	Pd – O 1.89–1.90 – C 1.89,1.90	Pd – O 2.09–2.14 – O 1.97	Pd – O 2.14 – C 2.01,2.02 C – O* 1.18	Pd – O 2.10–2.13 – O 2.15,2.23 O* – H 0.97	Pd – O 2.13–2.15 – C 2.13 C – H 1.11,1.12	Pd – O 2.13–2.15 – C 2.13,2.38 – H 1.25 C – H 1.11,1.12
Q_B	Pd −0.07, +0.15 H −0.16	Pd −0.06, +0.28 C −0.32	Pd +0.02, +0.24 O −0.79	Pd −0.04, +0.22 C +1.52 O* −1.88	Pd −0.03, +0.27 O* −1.51 H +1.00	Pd −0.04, +0.15 C −0.26 H +0.01, +0.04	Pd +0.11, +0.15 C −0.20 H −0.04, +0.06
pyr_{13}							
Site/adsorbate	H	C	O	OH	CO	CH_3	CH_3+H
tt Energy	2.98	5.42	4.2	2.12	2.13	2.28	dissociate
Pd – X	Pd – H 1.57	Pd – C 1.72	Pd – O 2.15–2.25 – O* 1.79	Pd – O 2.13–2.29 – O* 1.96 O – H 0.98	Pd – O 2.16–2.20 – C 1.86 C – O* 1.17	Pd – O 2.14–2.23 – C 2.03 C – H 1.10	Pd – O 2.16–2.28 – C 2.08 – H 1.00 C – H 1.10, 1.11
Q_B	H −0.08	C −0.08	Pd −0.07, +0.31 O* −0.66	Pd −0.07, +0.22 O* −1.43 H +1.00	Pd −0.10, +0.08 O* −1.88 C +1.75	Pd −0.12, +0.05 C −0.15 H −0.01, +0.05	Pd −0.13, +0.50 C −0.14 H −0.33, +0.04
tb Energy	3.23	6.87	4.35	2.36	2.05	2.24	−0.57
Pd – X	Pd – H 1.71, 1.73	Pd – C 1.80, 1.83	Pd – O 2.15–2.25 – O* 1.93, 1.94	Pd – O 2.13–2.28 – O* 2.11 O – H 0.97	Pd – O 2.14–2.25 – C 1.98, 2.00 C – O* 1.19	Pd – O 2.16–2.23 – C 2.06 C – H 1.10, 1.11	Pd – C 2.05 – H 1.55 C – H 1.10, 1.12
Q_B	H −0.11	C −0.22	Pd −0.07, +0.25 O* −0.69	Pd −0.11, +0.15 O* −1.46 H +1.00	Pd −0.09, +0.11 O* −1.88 C +1.66	Pd −0.12, +0.11 C −0.24 H −0.01, +0.09	Pd C −0.22 H −0.02, +0.07
th Energy	3.32	8.89	4.48	2.24	1.88	1.93	−0.75
Pd – X	1.81, 1.84	Pd – C 1.95–2.01	Pd – O 2.19–2.26 – O* 2.16–2.18	Pd – O 2.17–2.31 – O* 2.32, 2.33 O – H 0.98	Pd – O 2.15–2.23 – C 2.06 C – O* 1.20	Pd – O 2.13–2.22 – C 2.33 C – H 1.10, 1.11	Pd – C 2.09 – H 1.77 C – H 1.10, 1.11
Q_B	H −0.14	C −0.26	Pd −0.04, +0.14 O* −0.77	Pd −0.02, +0.11 O* −1.51 H +1.00	Pd −0.08, +0.07 O* −1.87 C +1.57	Pd −0.11, +0.13 C −0.52 H +0.07, +0.11	Pd C −0.12 H −0.10, +0.03
sbo Energy	3.72	8.35	5.16	3.29	2.65	2.29	dissociate
Pd – X	Pd – H 1.70, 1.76	Pd – C 1.79, 1.83	Pd – O 2.11–2.25 – O* 1.93, 1.94	Pd – O 2.13–2.27 – O* 2.06 O – H 0.97	Pd – O 2.14–2.27 – C 1.96, 1.98 C – O* 1.19	Pd – O 2.13–2.18 – C 2.08 C – H 1.10, 1.11	Pd – O 2.16–2.28 – C 2.08 – H 1.00 C – H 1.10, 1.11
Q_B	H −0.12	C −0.18	Pd −0.08, +0.38 O* −0.75	Pd −0.09, +0.27 O* −1.46 H +1.00	Pd −0.17, +0.15 O* −1.86 C +1.55	Pd −0.14, +0.15 C −0.11 H −0.07, +0.03	Pd −0.12, +0.04 C −0.21 H −0.37, +0.16
sbi Energy	3.4	8.13	5.10	2.23	2.18	2.22	dissociate
Pd – X	Pd – H 1.71, 1.76	Pd – C 1.86, 1.88	Pd – O 2.16–2.26 – O* 1.99–2.05	Pd – O 2.16–2.23 – O* 2.09 O – H 0.98	Pd – O 2.14–2.25 – C 1.96, 1.98 C – O* 1.19	Pd – O 2.15–2.19 – C 2.11, 2.35 C – H 1.10–1.13	Pd – C 2.10,2.35 – H 1.00 C – H 1.10, 1.13

Table 4 (*continued*)

pyr$_{13}$							
Site/adsorbate	H	C	O	OH	CO	CH_3	CH_3+H
Q_B	H −0.09	C −0.26	Pd −0.10, +0.37 O* −0.74	Pd −0.12, +0.30 O* −1.50 H +1.00	Pd −0.11, +0.15 O* −1.91 C +1.64	Pd −0.11, +0.15 C −0.25 H −0.01, +0.08	Pd C −0.14 H −0.35, +0.01 +0.78 bound wrt CH_4
sho Energy	3.68	8.06	4.99	3.16	3.4	2.63	
Pd–X	Pd–H 1.68, 1.77	Pd–C 1.84–1.89	Pd–O 2.16–2.23 –O* 1.99–2.17	Pd–O 2.13–2.29 –O* 2.08 O–H 0.98	Pd–O 2.15–2.24 –C 2.02–2.17 C–O* 1.20	Pd–O 2.15–2.19 –C 2.10, 2.28 C–H 1.10, 1.12	Pd–C 2.16, 2.19 C–H 1.10–1.13 Pd–H 1.70, 1.76
Q_B	H −0.12	C −0.26	Pd −0.13, +0.28 O* −0.75	Pd −0.09, +0.30 O* −1.46 H +1.00	Pd −0.12, +0.13 O −1.92 C +1.62	Pd −0.10, +0.09 C −0.35 H +0.03, +0.10	C −0.35 H −0.10, +0.08
shi Energy	3.45	8.12	5.1	2.52	2.36	2.22	−0.7
Pd–X	Pd–H 1.74,1.89	Pd–C 1.87,1.88	Pd–O 2.17–2.25 –O* 1.99–2.05	Pd–O 2.15–2.23 –O* 2.09 O*–H 0.97	Pd–O 2.15–2.29 –C 2.00–2.07 C–O 1.20	Pd–O 2.15–2.19 –C 2.07 C–H 1.10, 1.13	Pd–O 2.16–2.24 –C 2.07 –H 1.81 C–H 1.10, 1.11
Q_B	H −0.09	C −0.27	Pd −0.12, +0.39 O* −0.78	Pd −0.10, +0.30 O* −1.53 H +1.00	Pd −0.13, +0.19 O −1.90 C +1.64	Pd −0.11, +0.14 C −0.31 H +0.01, +0.09	Pd C −0.19 H −0.06, +0.03
she Energy	3.04	5.48	5.24	3.14	2.09	2.28	−0.56
Pd–X	Pd–H 1.57	Pd–C 1.73	Pd–O 2.16–2.24 –O* 1.94	Pd–O 2.13–2.27 –O* 2.07 O*–H 0.97	Pd–O 2.13–2.31 –C 1.85 C–O* 1.16	Pd–O 2.15–2.17 –C 2.10, 2.42 C–H 1.10–1.13	Pd–C 2.09 –H 1.57 C–H 1.09, 1.12
Q_B	H −0.09	C −0.15	Pd −0.09, +0.36 O* −0.75	Pd −0.13, +0.19 O* −1.45 H +1.00	Pd −0.10, +0.12 O* −1.82 C +1.64	Pd −0.10, +0.13 C −0.26 H −0.03, +0.09	Pd C −0.19 H −0.06, +0.08 +0.64 bound wrt CH_4
sbh Energy	3.27	8.14	5.09	1.85	2.05	1.63	
Pd–X	Pd–H 1.72, 1.74	Pd–C 1.86–1.87	Pd–O* 1.99–2.05	Pd–O 2.13–2.25 –O* 2.15 O*–H 0.99	Pd–O 2.15–2.26 –C 1.98, 1.99 C–O* 1.19	Pd–C 2.19–2.49 C–H 1.12–1.18	Pd–C >3 H–C 1.10
Q_B	H −0.08	C −0.21	Pd −0.12, +0.37 O* −0.75	Pd −0.10, +0.29 O* −1.50 H +1.00	Pd −0.11, +0.07 O* −1.85 C +1.63	C −0.41 H +0.05, +0.10	C −0.31 H −0.02, +0.16

space sampling) computational errors, we find the mid-gap reference state most convenient.

The atomic Bader charges for Pd associated with the most-favored sites show a +/− variation indicating the non-trivial charge flows associated with *atop*, *bridge*, and *hollow* adsorption geometries: H *atop* (−0.05, +0.06 e), C *hollow* (−0.05, +0.09 e), O *bridge* (−0.0, +0.30 e). These values can be compared with the calculated (−0.12, +0.13 e) variation in Pd charges on the clean Pd–STO interface. The associated charge transfers onto the ligand are H (−0.05 e) < C (−0.37 e) < O (−0.70 e).

4.2.3. 3-D atomic adsorption onto supported Pd particles

Atomic adsorption on the *pyr*$_5$ particle in the 3 × 3 × 1 surface model is reported in Table 4; here Pd–Pd *bridge* and *hollow* sites are energetically favored over the apical *atop* site. The maximal H, C, and O binding energies are respectively (0.91, 1.84, 0.45 eV) less than those of the most favorable sites on the 1 ML Pd films, indicating that *pyr*$_5$ is somewhat less capable of binding light atoms. The adsorption of atomic oxygen at different sites on the *pyr*$_5$ particle is shown in Fig. 8, reflecting the Pd–O* bond lengths of (1.78 < 1.92 < 1.97 Å) for *top*, *bridge*, and *hollow*, compared to the Pd–O substrate bonds of 2.09–2.19 Å.

Charge transfers onto the adsorbed atom follow the same scheme as seen for the 1 ML film: H *hollow* (−0.16 e) < C *hollow* (−0.32 e) < O *bridge* (−0.79 e). The range of Pd charge transfers is found as H (−0.07, +0.15 e), C (−0.06,+0.28 e), O (+0.01, +0.25 e); in every case the greatest Pd–X transfer is associated with the shortest Pd–X bond length, as would be expected.

Particle size effects and consequences of greater degrees of freedom can be observed in results for adsorption on a larger *pyr*$_{13}$ particle in the same 3 × 3 × 1 surface model, given in Table 4 and Fig. 8. Once again, Pd–Pd *bridge* sites are energetically favorable, with O cohesive energies ranging from 4.20 to 5.24 eV over the ten distinct sites surveyed. Of these, the apical *top–top* adsorption site is least favored, and a '*high-side-edge*' (*hse*) bridging site is most favored; Pd–O* bond lengths range from 1.79 Å '*top–top*' (*tt*) to 2.18 Å, the latter being also characteristic of Pd–O substrate bonds. The most-favored *hse* site displays an intermediate Pd–O* bond of 1.94 Å. Note that the maximal energy now exceeds that of adsorption on 1 ML Pd by 0.14 eV. The Pd–O charge transfers in this site: Pd (−0.09, +0.36 e) and O (−0.75 e) shows the same trend as discussed above, with larger absolute values; similar values are found for other low energy sites on this larger particle.

4.3. Molecular adsorption on zero-, two- and three-dimensional Pd

Adsorption of 'simple' molecular ligands on any surface is an obligatory starting point for both theoretical and experimental analyses of its chemical activity. Thus, by treating adsorption of small molecules (OH, CO, CH_3) onto supported Pd atoms, films and particles, it becomes possible to begin to sort out the inter-linked effects of substrate and topology upon chemical reactivity. Bearing in mind that partially oxidized Pd, and hydroxylated substrates are expected to play a role in catalytic processes, we also consider a limited number of cases of O and H coadsorption nearby the target molecules. Experimental studies of CO adsorption on Pd:nanocube STO are being undertaken [57]; catalytic activity of this system for the hydrogenation of acrolein has been reported [58]. Despite the complex ALD growth mechanism and somewhat complex processing of high-surface area nano-STO, it should be possible to make some comparisons between the present work and forthcoming experiments.

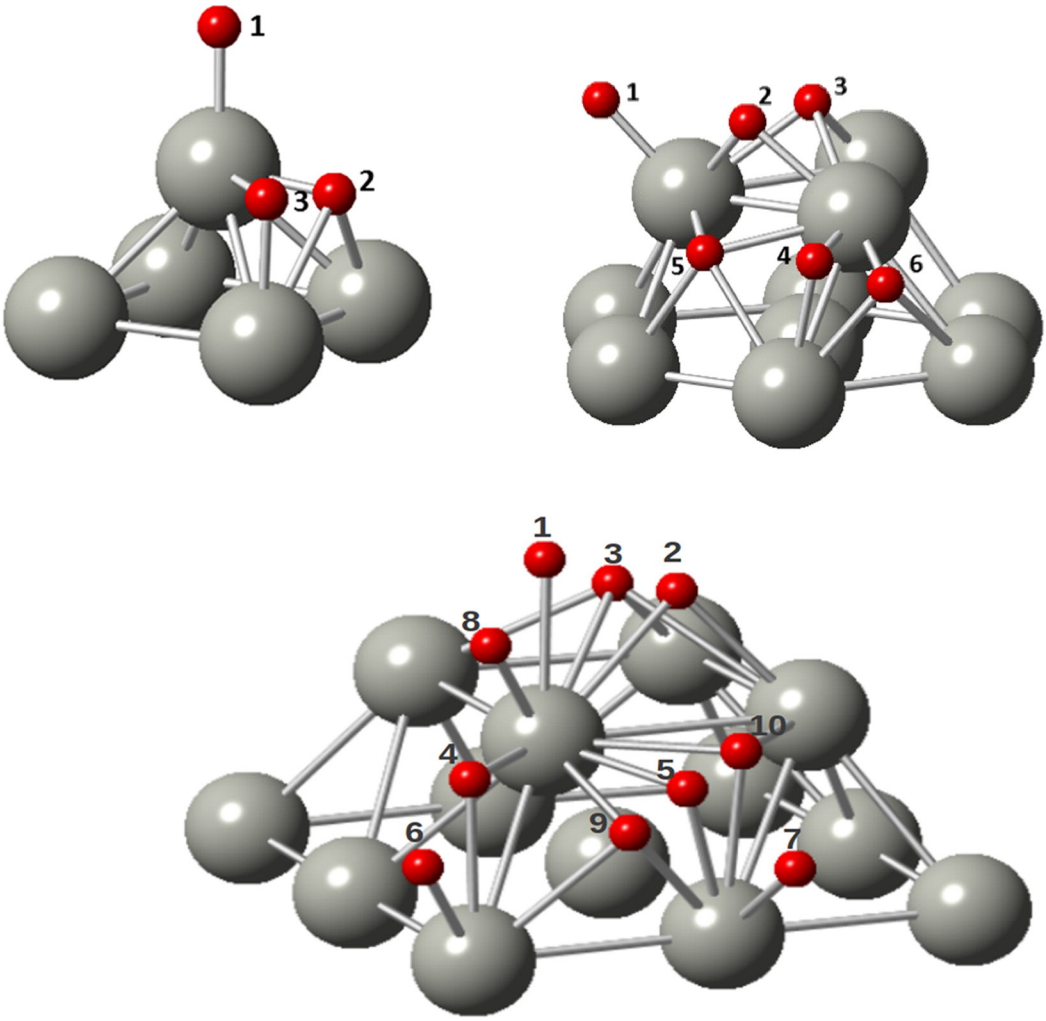

Fig. 8. Pyramidal pyr_5, pyr_{13} and hex_{10} models showing adsorption sites in red. The site numbering is correlated with site labels in text and tables as follows. pyr_5: *atop* (1), *hollow* (2), *bridge* (3). hex_{10}: *atop* (1), *bridge* (2, 3, 4), 4-fold *hollow* (5), 3-fold *hollow* (6). pyr_{13}: *atop* (1, 6, 7, 8), *bridge* (2, 4, 5), 3-fold *hollow* (9, 10), 4-fold *hollow* (3). Sites may be further characterized as *side-*, *high-*, *edge-*, etc. (For interpretation of the reference to color in this figure legend, the reader is referred to the web version of this article.)

4.3.1. OH molecular adsorption

Table 3 gives parameters of OH adsorption on Pd at 1/8 ML coverage in the 2 × 2 × 2 surface model. In the favored Pd-*bridge* configuration, a binding energy of 2.42 eV is favored over the Pd-*atop* site by ~0.3 eV. An O^* – Pd bond length of 1.98 Å is found, with a typical value of 0.98 Å found for the O^* – H bond. As is typical of odd-electron admolecules, the OH axis is predicted to be tipped, by ~45° relative to the (001) normal. Of course, OH^{-1} would be an *even* electron system, so the outcome is not obvious. The Bader charges are (−1.46, +1.00, +0.42 e) for O^*, H, and Pd respectively, showing a considerable charge transfer of ~0.37 e from Pd to the hydroxyl oxygen.

For 1 ML Pd in the 2 × 2 × 2 model (Table 3) we find that the Pd_2-*bridge* OH site (3.25 eV) is favored by ~0.2 and ~1.2 eV over the *atop*-Pd and 4-fold Pd-*hollow* positions. Coordination of O^* to two Pd atoms is seen to confer an additional ~0.8 eV of stability, compared to binding to one Pd. An O^* – Pd bond length of 2.12 Å is found, essentially equal to the 2.12–2.30 Å Pd distances to substrate oxygen. The O^* – H bond is again found as 0.98 Å. The Bader charges of (−1.44, +1.00, −0.06 to +0.24 e) for O^*, H and Pd show a hydroxyl distribution similar to that for adsorption on one Pd, and not surprisingly, with ~0.22 e being transferred from each bonded Pd to O^*.

Considering the pyr_5 particle in its most favorable configuration, OH adsorption is predicted to be most likely at the Pd_2-*bridge* location (as for 1 ML Pd), by 0.44 and 0.91 eV relative to *atop*-Pd and *hollow*-Pd_3 sites. The unrealistically large binding energy of 8.62 eV given in Table 4 is due to the convergence of the OH-in-gap reference state to a charged ion, as driven by equilibration of the Fermi energies of the two subsystems. The staggered $Pd_2 – O^*$ configuration gives bond lengths (2.04, 2.12 Å) slightly shorter than those of the Pd–O substrate, which range over 2.14–2.21 Å. Bader charges of (−1.58, +1.00, +0.01 to 0.35 e) for O^*, H, and Pd show a greater charge transfer to OH compared to the planar film results listed above.

Next consider the larger pyramidal particle pyr_{13} for which the site *sbo* (*side-bridge-outer*) is favored by 0.13–0.15 eV over *sho* (*side-hollow-outer*) and *she* (*side-high-edge*) sites, as shown in Table 4. Binding energies for the remaining eight sites considered are found to be considerably less, by 0.8 to 1.2 eV. As in the case of pyr_5, the OH-in-gap reference state converges to a charged hydroxyl $(O^*H)^{-0.41}$ which however, does not affect relative energy comparisons. The $Pd_2 – O^*$ bond length of 2.06 Å is comparable to those of the smaller particle, with the Pd – O substrate bonds of 2.13–2.27 Å again being typical, as is the O^* – H bond of 0.97 Å. The Bader charges of (–1.46, +1.0, −0.09 to +0.27 e) for O^*, H and Pd again show net transfer of ~0.5 e from bonded Pd to hydroxyl oxygen.

The 3 × 3 × 1 surface mesh with a hex_{10} particle provides the final example presented here: the *sht* (*side-high-tri*: 3-fold *hollow*) site for OH is favored by 0.13 eV over the *sb* (*side-bridge*) site; all other sites are more than 0.5 eV higher in energy (Table 5). The Pd – O^* bond

Table 5
Atom and molecule adsorption on supported hex_{10} cluster on TiO_2 terminated STO(100) in 3 × 3 × 1 substrate model. Pd_7 base is in registry to surface layer oxygen; adsorbate/molecular coverage corresponds to 1/9 ML; see text. Binding energies (eV) are given with respect to atom/relaxed molecule located at mid-gap between STO slabs with identical computational parameters. Site notation is: *top–top* (*tt*), *top-bridge* (*tb*), top-*hollow* (*th*), *side-bridge* (*sb*), *side-bridge-high* (*sbh*), *side-hollow-quad* (*shq*), *side-hollow-tri* (*sht*). Only stable sites are listed.

Site/energy	H	C	O	CO	OH	CH_3
tt	2.49	5.52	3.82	2.1	1.7	1.72
Energy						Partially dissociated
Pd–X	Pd–O 2.14–2.22 –H 1.54	Pd–O 2.15–2.23 –C 1.86	Pd–O 2.14–2.24 –O* 1.80	Pd–O 2.14–2.24 –C 1.80 C–O 1.20	Pd–O 2.14–2.22 –C 2.04 O–H 1.00	Pd–O 2.14–2.22 –C 1.88 –H 1.73, 1.74 C–H 1.10, 1.11
Q_B	Pd −0.07, +0.08 H −0.11	Pd −0.10, +0.10 C −0.13	Pd −0.05, +0.33 O −0.64	Pd −0.06, +0.07 O* −1.87 C +1.70	Pd −0.01, +0.21 O* −1.50 H +1.00	Pd −0.08, +0.14 C −0.22 H −0.11, +0.06
tb	2.78	6.55	4.15	1.64	1.92	2.25
Energy						
Pd–X	Pd–O 2.14–2.22 –H 1.85	Pd–O 2.16–2.29 –C 2.02	Pd–O 2.15–2.32 –O* 1.95	Pd–O 2.15–2.32 –C 1.95 C–O 1.12	Pd–O 2.14–2.22 –O* 2.06 O–H 1.00	Pd–O 2.15–2.31 –C 2.18, 2.22 C–H 1.10, 1.16
Q_B	Pd −0.04, +0.10 H −0.16	Pd −0.06, +0.12 C −2.54	Pd −0.01, +0.28 O −0.74	Pd −0.06, +0.09 O* −1.88 C +1.60	Pd −0.02, +0.17 O* −1.56 H +1.00	Pd −0.07, +0.08 C −0.31 H −0.02, +0.10
th	2.8	7.81	4.14	1.77	1.94	2.08
Energy						
Pd–X	Pd–O 2.14–2.22 –H >3	Pd–O 2.17–2.24 –C 1.87, 1.90	Pd–O 2.18–2.23 –O* 2.01, 2.06	Pd–O 2.18–2.24 –C 2.00, 2.07 C–O 1.20	Pd–O 2.14–2.22 –O* 2.07, 2.16 O–H 1.00	Pd–O 2.19–2.20 –C 2.11 C–H 1.10, 1.12
Q_B	Pd −0.05, +0.08 H −0.11	Pd −0.05, +0.09 C −0.31	Pd −0.02, +0.21	Pd −0.02, +0.09 O* −1.94 C +1.58	Pd −0.02, +0.15 O* −1.58 H +1.00	Pd −0.01, +0.16 C −0.35 H +0.02, +0.08
sb	2.42	8.67	4.89	2.42	2.51	2.8
Energy						
Pd–X	Pd–O 2.15–2.22 –H 1.81, 1.84	Pd–O 2.17–2.23 –C 1.87–1.92	Pd–O 2.16–2.26 –O* 1.92, 1.93	Pd–O 2.16–2.24 –C 1.94, 1.98 C–O 1.19	Pd–O 2.14–2.22 O* 2.06 O–H 1.00	Pd–O 2.15–2.24 –C 2.09, 2.24 C–H 1.11, 1.14
Q_B	Pd −0.13, +0.11 H −0.16	Pd −0.15, +0.10 C −0.33	Pd −0.12, +0.36 O* −0.72	Pd −0.14, +0.21 O* −1.86 C +1.64	Pd −0.10, +0.27 O* −1.52 H +1.00	Pd −0.13, +0.17 C −0.28 H −0.05, +0.11
sbh	3.42	7.13	4.16	1.63	2.51	2.44
Energy						Dissociated
Pd–X	Pd–O 2.15–2.22 –H 1.81, 1.84	Pd–O 2.13–2.30 –C 1.82	Pd–O 2.15–2.32 –O* 1.95	Pd–O 2.15–2.32 –C 1.94 C–O 1.20	Pd–O 2.15–2.22 –O* 2.02, 2.06 O*–H 1.00	Pd–O 2.16–2.27 –C 2.05, 2.13 –H 1.57–1.75 C–H 1.10
Q_B	Pd −0.13, +0.11 H −0.16	Pd −0.04, +0.10 C −0.30	Pd −0.02, +0.29	Pd −005, +0.10 O* −1.85 C +1.57	Pd −0.10, +0.27 O* −1.52 H +1.00	Pd −0.06, +0.19 C −0.46 H −0.12, +0.09
shq	2.07	8.76	4.20	2.15	1.91	1.96
Energy						
Pd–X	Pd–O 2.14–2.22 –H >3	Pd–O 2.17–2.26 –C 1.98–2.03	Pd–O 2.13–2.22 –O* 2.14	Pd–O 2.17–2.20 Pd–C 2.15, 2.20 C–O 1.22	Pd–O 2.15–2.23 –O* 2.32–2.43 O–H 0.97	Pd–O 2.13–2.28 –C 2.13, 2.28 C–H 1.11, 1.20
Q_B	Pd −0.12, +0.10 H −0.05	Pd −0.15, +0.18 C −0.41	Pd −0.11, +0.24 O −0.77	Pd −0.14, +0.17 O* −1.91 C +1.57	Pd −0.09, +0.23 O* −1.49 H +0.99	Pd −0.10, +0.14 C −0.26 H +0.02, +0.04
sht	2.34	8.78	4.68	2.41	2.64	2.59
Energy						Completely dissociated
Pd–X	Pd–O 2.14–2.22 –H >3	Pd–O 2.14–2.21 –C 1.89–1.98	Pd–O 2.16–2.24 –O* 1.93	Pd–O 2.16–2.23 Pd–C 1.94, 1.98 C–O 1.19	Pd–O 2.16–2.26 O* 2.11–2.13 O–H 1.01	Pd–O 2.17–2.35 –C 1.90–2.04 –H 1.65–1.74 C–H >3
Q_B	Pd −0.11, +0.11 H −0.14	Pd −0.14, +0.21 C −0.32	Pd −0.12, +0.37 O −0.73	Pd −0.13, +0.20 O* −1.87 C +1.65	Pd −0.05, +0.27 O* −1.47 H +0.99	Pd −0.20, +0.30 C −0.29 H −0.26, −0.10

length of 2.11 Å is a little larger than found for the 2-fold bridged sites reported above. The Pd–O (2.16–2.26 Å) and O*–H (1.01 Å) bonds are consistent with the preceding models. Bader charges of (−1.47, +0.10, −0.05 to 0.27 e) for O*, H and Pd confirm the nature and size of Pd to hydroxyl charge transfer in all cases studied.

4.3.2. CO molecular adsorption

Table 3 gives parameters of CO adsorption on Pd at 1/8 ML coverage in the 2 × 2 surface model. In the favored Pd-*atop* configuration, a binding energy of 2.48 eV and C–Pd bond length of 1.85 Å is found; the Pd-*bridge* state falls 0.07 eV higher in energy. A reasonable C–O bond length of 1.16 Å is found. Bader charges of (+1.81, −2.05, +0.26 e) for C, O*, and Pd show a polar CO group, with net charge of −0.24 e donated almost exclusively by its bound Pd.

For 1 ML Pd in the 2 × 2 model (Table 3) we find the Pd_2-*bridge* CO site to be favored, similar to OH. The *atop* and 4-fold *hollow* sites are uphill in energy by ~0.4 eV. In the 2-fold bridge configuration, the Pd–C bond length of 1.99 Å is somewhat larger than for the isolated Pd adsorption as would be expected. The CO bond length of 1.18 Å is similar to that of the *atop* case. Bader charges of (+1.66, −1.87, −0.07 to

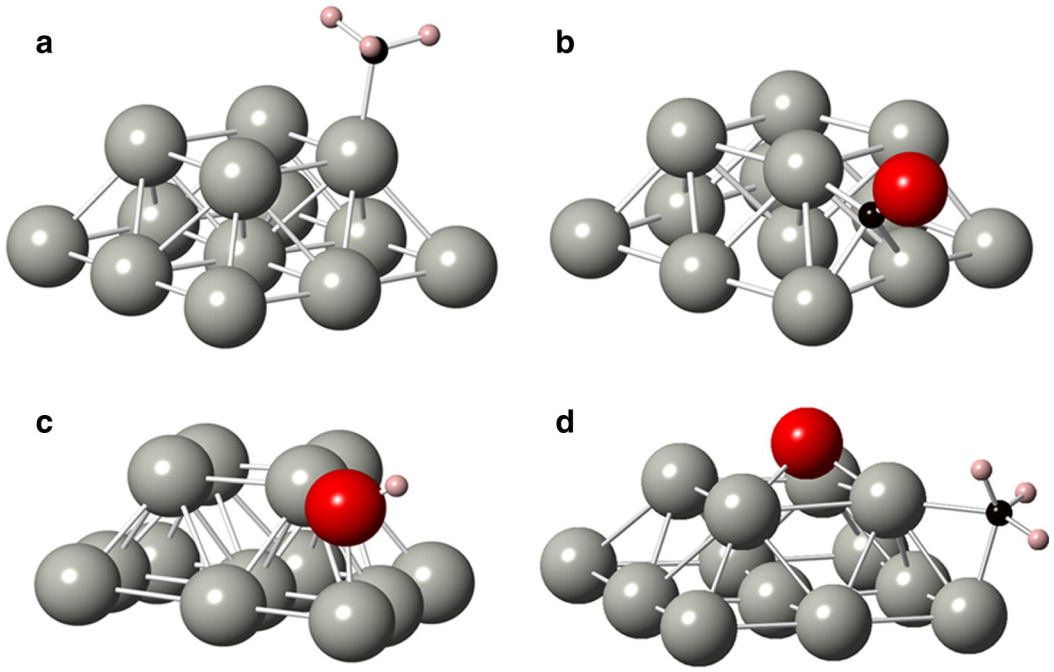

Fig. 9. Low energy molecular adsorption sites on pyr_{13} cluster, supported on (3 × 3 × 1) STO(001) substrate: (a) CH_3 *atop*, (b) CO *hollow*, (c) OH *bridge*, (d) CH_3 *bridge* + O *hollow*. Pd = gray, carbon = black, oxygen = red, hydrogen = pink. (For interpretation of the references to colors in this figure legend, the reader is referred to the web version of this article.)

+0.11) for C, O*, and Pd show the bridged CO to be slightly less polar, and the component atoms to be noticeably less ionic compared to *atop*.

Adsorption of CO on the pyr_5 cluster was modeled; energetics and geometric data are given in Table 4. The Pd_3-*hollow* site is found to be most stable, lying 0.1 and 0.9 eV below the 2-fold *bridge* and 1-fold *atop* sites. With increasing coordination, the Pd – C bond lengths again increase, to 2.01–2.02 Å, while the CO bond remains at 1.18 Å. The Bader charges (+1.52, −1.88, −0.04 to +0.22) for C, O*, and Pd show CO to be more ionic in this configuration than either of the film geometries discussed above.

The larger pyramidal particle pyr_{13} (Table 4) again reveals a strong CO preference for 3-fold Pd_3-*hollow* sites. The *sho* (*side-hollow-outer*) site is favored by 0.75, 1.04 eV over the 2-fold *sbo* (*side-bridge-outer*) and 3-fold *shi* (*side-hollow-inner*) sites respectively. Pd – C bond lengths range over 2.02–2.17 Å, with CO relaxing a bit to 1.20 Å. Bader charges of (+1.62, −1.92, −0.12 to +0.13) for C, O*, and Pd reveal a charged $CO^{-0.3}$ group, and with the larger electron reservoir of the Pd_{13} particle, a less perturbed metal donor.

The hexagonal hex_{10} particle (Table 5) shows two sites with nearly identical greatest binding: 2-fold *sb* (*side-bridge*) and 3-fold *sht* (*side-hollow-tri*). 4-fold *hollow* and top-most *atop* sites followed by ~0.3 eV in energy ranking. The *sb* site reveals Pd – C bond lengths of 1.94 and 1.98 Å, with a CO bond of 1.19 Å. Bader charges of (+1.64, −1.86, −0.14 to +0.21 e) for C, O*, and Pd show the now familiar distribution, with CO net charge of −0.22 e.

4.3.3. CH_3 molecular adsorption

Table 3 gives parameters of CH_3 adsorption on Pd at 1/8 ML coverage in the 2 × 2 surface model. In the favored Pd–*bridge* configuration, binding energy of 2.37 eV and Pd – C bond length of 2.03 Å are found. The C – H bond lengths of 1.10–1.11 Å and Bader charges of (−0.15, −0.01 to +0.01, +0.22 e) for C, H, and Pd set reference values for comparison with adsorption on more dense Pd conformations. Table 3 also gives comparable data for adsorption on 1 ML coverage; with binding energy of 2.91 eV for the favored *atop* site, with the 2-fold *bridge* site lying 0.15 eV higher. The 4-fold *hollow* site lies 0.9 eV above the *atop* configuration. The *atop* Pd – C, and C – H bond lengths are 2.02, and 1.10 Å respectively, with Bader charges (−0.27, +0.01 to +0.14, −0.06 to +0.22 e) for C, H, and Pd.

Adsorption on pyr_5 is reported in Table 4; here the favored *bridge* configuration has an energy of 2.35 eV, lying 0.1 and 0.3 eV below *atop* and 3-fold *hollow* sites respectively. The *bridge* Pd – C and C – H bond lengths are 2.05 and 1.10 to 1.13 Å, the 2-fold coordination to Pd leading to slightly relaxed bonds. Bader charges of (−0.27, 0.0 to +0.07, −0.05 to +0.18 e) for C, H, and Pd show the same general characteristics and values as for planar adsorption discussed above.

Data for the pyr_{13} adsorption are also given in Table 4, showing the 3-fold *sho* site, with binding energy 2.63 eV, to be most favored. The 2-fold and alternate 3-fold sites follow, clustered ~0.3 eV higher, with the 4-fold *hollow* being least favored of all. In *sho*, the Pd – C and C – H bond lengths are 2.20–2.28 Å and 1.10–1.12 Å respectively, showing a further relaxation with increasing Pd coordination. Bader charges (−0.35, +0.03 to +0.10, −0.10 to +0.09 e) for C, H, and Pd report an electronic distribution slightly more polar than found for 1- and 2-fold coordination.

The hexagonal hex_{10} particle (Table 5) shows the *sb* (*side-bridge*) configuration at the lowest energy, followed by 3-fold *sht* 0.2 eV higher. Following another bridging site *sbh* at 0.37 eV, the remaining configurations fall at higher energy ranging from 0.6 to 1.0 eV. For *sb* the Pd – C bond lengths are 2.09, 2.24 Å with C – H bonds at 1.11, and 1.14 Å. Bader charges are (−0.28, −0.05 to +0.11, −0.13 to +0.17 e) for C, H, and Pd following a trend seen for the other particles.

4.3.4. CH_3 molecular co-adsorption with H and O

By considering the co-adsorption of methyl and H we may examine some of the 'end points' of the process by which CH_4 dissociates in interaction with Pd. Treating the full potential surface for incoming methane upon the Pd_N overlayers and particles is well beyond the scope of this work. However, insights may be gained by taking snapshots of some possible initial, intermediate and final states. Similarly, in view of the apparent activation of Pd metal as a catalyst in partial oxidation, study of the methyl–oxygen interaction on Pd can be revealing. Fig. 9d shows a typical relaxed geometry for CH_3 + O on a low-energy *sho* site of the pyr_{13} particle. Due to its limited bonding capability, H migrates to a staggered *bridge* site, while O prefers

the nearby 3-fold hollow as shown. The energetics show that coadsorption of CH_3 and O, at 7.28 eV is *not* favored over independent adsorption on separate, minimum energy sites (7.87 eV) so no thermodynamic driving force is present. On the other hand, if oxygen is already present (as is highly likely), methyl adsorption is still highly favored.

As methane is believed to spontaneously dissociate in contact with Pd, it is not surprising that attempts to form closely linked CH_3+H complexes generally failed. For the pyr_{13} model, only the *sho* site was found to be stable relative to CH_4 in the vacuum-slab gap, and by only 0.22 eV. In this case the methyl Pd–C and C–H bond lengths are reasonable (2.15–2.19, 1.10–1.14) Å while the fourth hydrogen is loosely coupled to methyl with a C–H distance of 1.61 Å. The methyl H are positive (+0.08 e) while the weakly bound H is anionic (−0.10 e). Of course, well-separated methyl and an additional H–Pd pair are quite stable. These data suggest that it would be interesting to map out a static energy landscape for the CH_3+H complex on and around the metal particles. Such a study is however, beyond the scope of the present work.

5. Summary and conclusions

The general state of knowledge is that particle topological features, just like surface steps, edges, and kinks provide active metal sites for chemisorption and subsequent catalytic reactions. The present work has explored the structural stability and energetics of a number of Pd_N particles with structure found experimentally upon STO(001) surfaces, and which are known to exhibit catalytic response. By comparison with low and moderate coverage 0D and 2D metal films on the oxide substrate, we have been able to quantitatively compare and contrast features of electronic structure and resulting chemical properties as measured by adsorption of atoms and small molecules upon the 3D particles.

In the following energy comparisons, it is good to bear in mind the unavoidable differences between reference states in some cases, and the limitations of the DFT potentials used in general.

Using the $2\times2\times2$ surface model as an example of 2D configurations, we find the lowest energies for 1/8-, 1/4-, 1/2-, and 1 ML Pd coverages as 1.48 < 1.69 < 1.98 < 2.53 eV/Pd respectively. This clearly demonstrates the cohesive attraction of Pd–Pd interactions on the surface, stabilizing larger rafts and particles. A further indication of the relative importance of Pd–Pd interactions is found by comparing two geometries of the 1/2 ML coverage: compact ribbon vs dispersed structure shows an advantage of 0.36 eV/Pd for the compact structure. The Pd–O bond lengths follow a similar trend: 2.05 < 2.07 < 2.14 < 2.22 Å indicating a qualitative weakening of the metal–substrate interaction with increasing metal concentration. Pd Bader charges of 0.05, −0.04 to +0.04, −0.04 to +0.02, and −0.12 to +0.13 e reveal a steadily increasing charge transfer between substrate and adsorbate with increasing coverage; this along with increasing bond lengths suggests an increasing ionic bonding characteristic.

Moving from 2D to 3D Pd_N supported particles, recall that the most favored sites maximize Pd–O bonding, and that the surface oxygen mesh is square with nearest O–O distance of $a/\sqrt{2} = 2.761$ Å. The simplest pyr_5 particle with square base relaxes (in the $2\times2\times2$ model) to a Pd–Pd basal-plane distance of 2.65 Å and base-apex bond of 2.67 Å, representing a compressive strain of 4% on the substrate surface-layer. The surface O aligns with Pd; the cohesive energy of 2.35 eV/Pd is intermediate between that of 1/2- and 1 ML films, with Pd–O bond length of 2.14 Å identical to that of 1/2 ML. A notable difference is seen in the Pd Bader charges, which increase in magnitude, −0.28 to +0.19 e.

Turning to a larger pyramid pyr_{13} in the $(3\times3\times2)$ model we find an expected increased stability, 2.78 eV/Pd with a 9 atom base which is not perfectly planar. Basal Pd–O distances range from 2.13 to 2.18 Å, slightly relaxed compared to pyr_5. The base–base Pd bond lengths, 2.64–2.69 Å, the base-plateau lengths of 2.64–2.82 Å, and plateau–plateau lengths of 2.79–2.81 Å all show a tendency to relax toward the Pd metallic value with increasing size, and distance from the substrate. The hex_{10} and hut_8 particles confirm these trends, with minor quantitative differences. Thus it is apparent that the so-called strong metal–substrate interaction is largely confined to the contact layer, weakening rapidly for metal sites with distance from the interface. As measured by the Bader partitioning, the magnitude of charge transfer between substrate and particle, and within particle atoms reaches a few tenths of e, with Pd closest to O becoming most positively charged as would be expected.

Atomic adsorption onto relatively isolated Pd and onto Pd_N particles shows systematic trends: let us turn first to oxygen, since it is known to influence the catalytic activity of the metal. The calculated binding energy per O is 3.79 < 4.65 < 4.89 < 5.10 < 5.24 eV for 1/8 ML, pyr_5, hex_{10}, 1 ML, and pyr_{13} binding respectively. In general oxygen is found to prefer 2-fold *bridge* sites, although obviously the geometries vary from one case to another. The corresponding Pd–O^* bond lengths are 1.82, 1.92, 1.92, 1.98, and 1.94 Å with oxygen Bader charges of −0.69, −0.79, −0.72, −0.70, and −0.75 e showing a moderate trend toward greater bond length with greater binding energy, perhaps contrary to expectation. The adsorbate O^* has considerably less charge than that of substrate oxygen — ranging typically from −1.1 to −1.3 e.

With its limited bonding capacity, H tends to prefer *atop* and staggered *bridge* sites, while polyvalent C seeks multiple Pd–C coordination, choosing *hollow* sites where available. Thus, energies for H adsorption are found to be 2.78 (hex_{10} *top*) < 3.25 (pyr_5 *hollow*) < 3.78 (1/8 ML *top*) < 4.16 eV(1 ML *top*), both particles calculated in the $3\times3\times1$ model. The corresponding Pd–H bond lengths of 1.85, 1.73, 1.58, 1.61 Å suggest delocalized bonding, with H Bader charges of −0.16, −0.16, −0.17, and −0.05 e showing formation of a weak anion. For carbon we find 4.79 (1/8 ML *top*) < 7.31 (pyr_5 *hollow*) < 7.81 (hex_{10} *hollow*) < 9.15 eV(1 ML *top*), with the unrealistically large values being due to a charged C-slab reference state described previously. The corresponding Pd–C bond lengths of 1.76, 1.89, 1.87, and 1.97 Å and C Bader charges of −0.18, −0.32, −0.31, and −0.37 e suggest a mixture of ionic and covalent bonding, with greater ionicity associated with greater bond length, as seen in Pd–O^* interactions.

We summarize here the results and conclusions for adsorption of CO, the experimental favorite, on pyr_5, pyr_{13}, and hex_{10} in the most favored configurations. CO binding energies are respectively 2.01 < 2.42 < 3.40 eV for 5-, 10-, and 13-atom Pd particles in 3-fold, *bridge*, and 3-fold *hollow* sites. The corresponding Pd–C and C–O^* bond lengths are (2.01–2.02, 1.20), (1.94–1.98, 1.19) and (2.02–2.17, 1.20) Å while the C, O^* Bader charges are (+1.52, −1.88), (+1.64, −1.86) and (+1.62, −1.92)e respectively. A consistent picture thus arises of binding increasing systematically with particle size, and thus with variety of site topologies available. The shortest Pd–C bond lengths of 1.94 to 2.02 Å and the net CO charges of −0.22 to −0.36 e are compatible with a moderately strong covalent bond to the metal. The resulting CO dipole moment points from O^* toward C, as would be expected.

Assaying the OH data presented in a previous section similarly, one sees molecular cohesive energies of 8.62, 2.64 and 3.29 eV for 5-, 10-, and 13-atom particles in *bridge*, *hollow*, and *bridge* sites respectively. The anomalously large value for OH at pyr_5 is due to a highly charged (−0.54 e) OH-in gap reference state induced by Fermi statistics. A correction of that value to a common reference would pull it back into conformity with the general trend. The respective Pd–O^*, and O^*–H bond lengths are pyr_5 (2.04–2.12, 0.97), hex_{10} (2.11–2.13, 1.01) and pyr_{13} (2.06, 0.97) Å with corresponding O^*, H Bader charges of (−1.58, +1.0), (−1.46, +1.0) and (−1.47, +0.99)e respectively. The shortest metal–O^* bonds of 2.04–2.11 Å and the net O^*H charges of −0.46 to −0.58 e lead to a characterization of the hydroxyl bond as being somewhat more ionic than that of CO.

In the same manner, we summarize methyl on Pd_N as follows: cohesive energy 2.35, 2.80, and 2.63 eV on 5-, 10- and 13-atom supported

particles, in *bridge*, *bridge*, and *hollow* configurations. CH_3 reveals a number of partial or totally dissociated states at relatively low energies on other sites; all of these are of higher energy than the stable sites just mentioned. Pd – C bond lengths of pyr_5 2.05, hex_{10} 2.09–2.24, pyr_{13} 2.10–2.28 Å and C – H bonds of 1.10–1.13, 1.11–1.14, and 1.10–1.12 Å are found, respectively. The Pd – C bond is thus systematically longer in methyl than in CO; the C – H bonds are likewise longer than the O – H bonds, all as expected. Very limited studies of CH_3 coadsorption with O and H were made, to obtain some idea about cooperative effects. On pyr_{13} it was found that preadsorbed O reduces the binding energy of close-by methyl by ~0.5 eV; on the other hand the CH_3 + H interaction might be called repulsive at short separations. Any CH_3 + H complex assembled on the Pd particle relaxed to a weak association, or a dissociated state.

To summarize our results grosso modo: Relaxed chemical structures involving Pd_N:STO(001) show features expected on the basis of 'cartoon models' developed from chemical intuition and limited experimental data, now expressed in quantitative form. Model systems such as those presented here, in combination with atomic-scale synthesis and analysis, may be expected to lead to more stable, selective and highly reactive catalysts. In view of recent experimental measurements, showing variation in particle morphology, and catalytic activity/selectivity with substrate chemistry, further studies of supported Pt and Ag nanoparticles are planned, using mixed-perovskite substrates such as $Sr_{1-x}Ba_xTiO_3$.

Acknowledgments

This research was supported in part by the Chemical Sciences, Geosciences and Biosciences Division, Office of Basic Energy Sciences, Office of Science, the US Department of Energy, Grant No. DE-FG02-03ER15457, at the Institute for Catalysis in Energy Processes at Northwestern University.

References

[1] S.T. Christensen, J.W. Elam, B. Lee, Z. Feng, M.J. Bedzyk, M.C. Hersam, Chem. Mater. 21 (2009) 516.
[2] S.T. Christensen, J.W. Elam, F.A. Rabuffetti, Q. Ma, S.J. Weigand, B. Lee, S. Seifert, P.C. Stair, K.R. Poeppelmeier, M.C. Hersam, M.J. Bedzyk, Small 5 (2009) 750.
[3] F. Silly, A.C. Powell, M.G. Martin, M.R. Castell, Phys. Rev. B 72 (2005) 165403.
[4] Z. Zhang, J. Feng, Z. Wang, F. Yang, Q. Guo, J. Chem. Phys. 135 (2011) 144702.
[5] (a) W. Kohn, L.J. Sham, Phys. Rev. 140 (1965) 1133;
(b) J.P. Perdew, J.A. Chevary, S.H. Vosko, K.A. Jackson, M.R. Pederson, D.J. Singh, C. Fiolhais, Phys. Rev. B 46 (1992) 6671;
(c) J.P. Perdew, K. Burke, M. Ernzerhof, Phys. Rev. Lett. 77 (1996) 3865 (ibid Erratum 78 (1997) 1396);
(d) J.P. Perdew, A. Ruzsinszky, G.I. Csonka, O.A. Vydrov, G.E. Scuseria, L.A. Constantin, X.L. Zhou, K. Burke, Phys. Rev. Lett. 100 (2008) 136406.
[6] P. Haas, F. Tran, P. Blaha, Phys. Rev. B 79 (2009) 085104.
[7] W. Qi, B. Huang, M. Wang, Nanoscale Res. Lett. 4 (2009) 269.
[8] P. Nava, M. Sierka, R. Ahlrichs, Phys. Chem. Chem. Phys. 5 (2003) 3372.
[9] J. Rogan, G. Garcia, M. Ramirez, V. Munoz, J.A. Valdivia, X. Andrade, R. Ramirez, M. Kiwi, Nanotechnology 19 (2008) 205701.
[10] B.C. Bolding, E.A. Carter, Phys. Rev. B 42 (1990) 11380.
[11] D. Tomanek, Z. Sun, S.G. Louie, Phys. Rev. B 43 (1991) 4699.
[12] T. Ochs, S. Köstlmeier, C. Elsässer, Integr. Ferroelectr. 32 (2001) 959 (ibid, MRS Proc. (2000) 654: AA3.4.1).
[13] T. Ochs, C. Elsässer, Z. Metallkd. 93 (2002) 406.
[14] S. Abbet, A.M. Ferrari, L. Giordano, G. Pacchioni, H. Hakkinen, U. Landman, U. Heiz, Surf. Sci. 514 (2002) 249.
[15] J. Hoffmann, S. Schauermann, V. Johanek, H. Unterhalt, G. Rupprechter, J. Libuda, H.-J. Freund, J. Phys. Chem. B 107 (2003) 255.
[16] L. Piccolo, C.R. Henry, J. Mol. Catal. A Chem. 167 (2001) 181.
[17] S.L. Tait, Z. Dohnalek, C.T. Campbell, B.D. Kay, Surf. Sci. 591 (2005) 90.
[18] (a) I. Atanasov, G. Barcaro, F.R. Negreiros, A. Fortunelli, R.L. Johnston, J. Chem. Phys. 138 (2013) 224703;
(b) Paola Nava, Marek Sierka, Reinhart Ahlrichs, Phys. Chem. Chem. Phys. 5 (2003) 3372;
(c) S.M. Kozlov, H.A. Aleksandrov, J. Goniakowski, K.M. Neyman, J. Chem. Phys. 139 (084701) (2013);
(d) J. Goniakowski, A. Jelea, C. Mottet, G. Barcaro, A. Fortunelli, Z. Kuntová, F. Nita, A.C. Levi, G. Rossi, R. Ferrando, J. Chem. Phys. 130 (2009) 174703;
(e) W. Vervisch, C. Mottet, J. Goniakowski, Phys. Rev. B65 (2002) 245411;
(f) E. Apra', A. Fortunelli, J. Mol. Struct. Theochem. 501–502 (2000) 251;
(g) G. Barcaro, A. Fortunelli, G. Rossi, F. Nita, R. Ferrando, Phys. Rev. Lett. 98 (2007) 156101;
(h) N. Lopez, F. Illas, N. Rösch, G. Pacchioni, J. Chem. Phys. 110 (1999) 4873;
(i) G. Barcaro, A. Fortunelli, J. Chem. Theory Comput. 1 (2005) 972.
[19] Yu F. Zhukovskii, E.A. Kotomin, D.E. Ellis, Phys. Stat. Sol. B 245 (2008) 980.
[20] (a) G.L. Haller, D.E. Resasco, Adv. Catal. 36 (1989) 173;
(b) X.E. Verykios, in: A. Wieckowski, E.R. Savinova, C.G. Vayenas (Eds.), Catalysis and Electrocatalysis at Nanoparticle Surfaces, CRC Press, 2003;
(c) B. Coq, F. Figueras, in: A. Wieckowski, E.R. Savinova, C.G. Vayenas (Eds.), Catalysis and Electrocatalysis at Nanoparticle Surfaces, CRC Press, 2003.
[21] (a) J.H. Sinfelt, J. Phys. Chem. 68 (1964) 344;
(b) W.F. Taylor, D.J.C. Yates, J.H. Sinfelt, J. Phys. Chem. 68 (1964) 2962;
(c) W.F. Taylor, J.H. Sinfelt, D.J.C. Yates, J. Phys. Chem. 69 (1965) 3857;
(d) D.J.C. Yates, J.H. Sinfelt, W.F. Taylor, Trans. Faraday Soc. 61 (1965) 2044.
[22] N.D. Spencer, R.C. Schoonmaker, G.A. Somorjai, Nature 294 (1981) 643.
[23] G. Wulff, Z. Krystallogr. Mineral. 34 (1901) 449.
[24] G. Richter, T. Wagner, J. Appl. Phys. 98 (2005) 094908.
[25] H. Iddir, V. Komanicky, S. Ogut, H. You, P. Zapol, J. Phys. Chem. C 111 (2007) 14782.
[26] J.A. Enterkin, W. Setthapun, J.W. Elam, S.T. Christensen, F.A. Rabuffetti, L.D. Marks, P.C. Stair, K.R. Poeppelmeier, C.L. Marshall, ACS Catal. 1 (2011) 629.
[27] J.A. Enterkin, K.R. Poeppelmeier, L.D. Marks, Nano Lett. 11 (2011) 993.
[28] (a) M. von Laue, Z. Kristallogr. 105 (1943) 124;
(b) A. Dinghas, Z. Kristallogr. 105 (1943) 304;
(c) C. Herring, Phys. Rev. 82 (1951) 87.
[29] W.L. Winterbottom, Acta Metall. 15 (1967) 303.
[30] R. Kaischew, Arbeitstagung Festkörper Physik, 1952. 81 (Dresden).
[31] C.R. Henry, Prog. Surf. Sci. 80 (2005) 92.
[32] (a) Y. Takasu, R. Unwin, B. Tesche, A.M. Bradshaw, Surf. Sci. 77 (1978) 219;
(b) R. Unwin, A.M. Bradshaw, Chem. Phys. Lett. 58 (1978) 58;
(c) M. Gillet, A. Renou, Thin Solid Films 52 (1978) 23 (DURING GROWTH ON AN MoS 2 SUBSTRATE);
(d) A. Moore, V. Celorrio, M.M. de Oca, D. Plana, W. Hongthani, M.J. Lazaro, D.J. Fermin, Chem. Commun. 47 (2011) 7656;
(e) K. Ding, Int. J. Electrochem. Sci. 5 (2010) 668.
[33] N. Erdman, K.R. Poepplemeier, M. Asta, O. Warschkow, D.E. Ellis, L.D. Marks, Nature 419 (2002) 55 (and references therein).
[34] (a) D.S. Deak, Mater. Sci. Technol. 23 (2007) 127;
(b) B.C. Russell, M.R. Castell, Phys. Rev. B 77 (2008) 245414;
(c) R.I. Eglitis, D. Vanderbilt, Phys. Rev. B 77 (2008) 195408;
(d) L.D. Marks, A. Chiaramonti, F. Tran, P. Blaha, Surf. Sci. 603 (2009) 2179;
(e) J.A. Enterkin, A.K. Subramanian, B.C. Russell, M.R. Castell, K.R. Poeppelmeier, L.D. Marks, Nat. Mater. 9 (2010) 245.
[35] M. Bedzyk, et al., private communication, 2014.
[36] G. Kresse, J. Furthmüller, Phys. Rev. B 54 (1996) 11169.
[37] G. Kresse, J. Furthmüller, Comput. Mater. Sci. 6 (1996) 15.
[38] G. Kresse, J. Hafner, Phys. Rev. B 47 (1993) 558.
[39] G. Kresse, J. Hafner, Phys. Rev. B 49 (1994) 14251.
[40] I. de P.R. Moreira, F. Illas, R.L. Martin, Phys. Rev. B 65 (2002) 155102.
[41] N.C. Wilson, S.P. Russo, Phys. Rev. B 79 (2009) 094113.
[42] H.J. Monkhorst, J.D. Pack, Phys. Rev. B 13 (1976) 5188.
[43] (a) J.J. Jin, X.Y. Ma, C.-Y. Kim, D.E. Ellis, M.J. Bedzyk, Surf. Sci. 601 (2007) 3082;
(b) J.J. Jin, X.Y. Ma, C.-Y. Kim, D.E. Ellis, M.J. Bedzyk, Surf. Sci. 601 (2007) 4571.
[44] M.E. McBriarty, M.J. Bedzyk, D.E. Ellis, Surf. Sci. 606 (2012) 1367.
[45] (a) R.F.W. Bader, Atoms in Molecules: A Quantum Theory, Clarendon Press, Oxford, 1990.;
(b) G. Henkelman, A. Arnaldsson, H. Jónsson, Comput. Mater. Sci. 36 (2006) 354.
[46] (a) M.H. Shao, T. Huang, P. Liu, J. Zhang, K. Sasaki, M.B. Vukmirovic, R.R. Adzic, Langmuir 22 (2006) 10409;
(b) M. Takahasi, Y. Hayashi, J. Mizuki, K. Tamura, T. Kondo, H. Naohara, K. Uosaki, Surf. Sci. 461 (2000) 213;
(c) Sh.K. Shaikhutdinov, R. Meyer, D. Lahav, M. Bäumer, T. Klüner, H.-J. Freund, Phys. Rev. Lett. 91 (2003) 76102;
(d) A.W. Potts, G.R. Morrison, L. Gregoratti, M. Kiskinova, A. Locatelli, Phys. Rev. B 67 (2003) 045411.
[47] (a) J. Ihm, M.L. Cohen, J.R. Chelikowsky, Phys. Rev. B 22 (1980) 4610;
(b) M.J. Zhu, D.M. Bylander, L. Kleinman, Phys. Rev. B 42 (1990) 2874;
(c) M.I. Rojas, M.G. Del Pópolo, E.P.M. Leiva, Langmuir 16 (2000) 9539;
(d) O.V. Stepanyuk, P.A. Ignatiev, N.N. Negulyaev, A.M. Saletsky, W. Hergert, J. Phys. Condens. Matter 24 (2012) 235301.
[48] (a) M. Baldauf, D.M. Kolb, Electrochim. Acta 38 (1993) 2145;
(b) W.K. Kuhn, J. Szanyi, D.W. Goodman, Surf. Sci. 274 (1992) L611;
(c) J. Szanyi, W.K. Kuhn, D.W. Goodman, J. Vac. Sci. Technol. A11 (1969) (1993);
(d) E.L. Wilson, W.A. Brown, G. Thornton, Surf. Sci. 600 (2006) 2555;
(e) W.E. Kaden, W.A. Kunkel, F.S. Roberts, M. Kane, S.L. Anderson, J. Chem. Phys. 136 (2012) 204705;
(f) S. Nagarajan, K. Thirunavukkarasu, C.S. Gopinath, S.D. Prasad, J. Phys. Chem. 115 (2011) 15487;
(g) I. Bakó, R. Schennach, G. Pálinkás, J. Phys. Conf. Ser. 100 (2008) 052067;
(h) B. Hammer, Phys. Rev. Lett. 89 (2002) 16102.
[49] (a) G.W. Simmons, Y.-N. Wang, J. Marcos, K. Klier, J. Phys. Chem. 95 (1991) 4522;
(b) Y. Zhang, J. Rogal, K. Reuter, Phys. Rev. B74 (2006) 125414.
[50] N. Erdman, O. Warschkow, K.R. Poeppelmeier, M. Asta, D.E. Ellis, L.D. Marks, J. Am. Chem. Soc. 125 (10050) (2003) 10050.
[51] O. Warschkow, N. Erdman, K.R. Poeppelmeier, D.E. Ellis, L.D. Marks, Surf. Sci. 573 (2004) 446.
[52] (a) F.H. Ribeiro, M. Chow, R.A. Dalla Betta, J. Catal. 146 (1994) 537;

(b) E. Garbowski, C. Feumi-Jantou, N. Mouaddib, M. Primet, Appl. Catal. A 109 (1994) 277;
(c) T. Maillet, C. Solleau, J. Barbier Jr., D. Duprez, Appl. Catal. B 14 (85) (1997) 85;
(d) D. Ciuparu, M.R. Lyubovsky, E. Altman, L.D. Pfefferle, A. Datye, Catal. Rev. Sci. Eng. 44 (2002) 593.
[53] G.T. de Jong, M. Sola, L. Visscher, F.M. Bickelhaupta, J. Chem. Phys. 121 (2004) 9982.
[54] Q. Cui, D.G. Musaev, K. Morokuma, J. Phys. Chem. A 102 (1998) 6373.
[55] (a) M.-S. Liao, C.-T. Au, C.-F. Ng, Chem. Phys. Lett. 272 (1997) 445;
(b) Y. Akinaga, T. Taketsugu, K. Hirao, J. Chem. Phys. 109 (1998) 11010.
[56] A. Hellman, A. Resta, N.M. Martin, J. Gustafson, A. Trinchero, P.-A. Carlsson, O. Balmes, R. Felici, R. van Rijn, J.W.M. Frenken, J.N. Andersen, E. Lundgren, H. Grönbeck, J. Phys. Chem. Lett. 3 (2012) 678.
[57] P. Stair, private commun, 2014.
[58] K.R. Poeppelmeier, et al., private commun, 2014.